On the fatigue propagation of multiple cracks in friction stir weldments using linear and non-linear models under cyclic tensile loading

Marcello Lepore[a,*], Filippo Berto[b]

[a] Department of Industrial Engineering, University of Salerno, Via G. Paolo II 132, 84084 Fisciano (SA), Italy
[b] Department of Mechanical and Industrial Engineering, NTNU, Richard Birkelands vei 2b, 7491 Trondheim, Norway

A B S T R A C T

In this work, the propagation life of a friction stir-welded sample made of ductile materials is estimated by employing linear elastic fracture mechanics (LEFM) and small-scale yielding (SSY) conditions. The purpose is to demonstrate that by considering the SSY, the prediction of the propagation life of the welded sample can be improved when compared to the traditional LEFM. The process of friction stir welding (FSW) of an AA2024-T3 butt joint is then simulated by using the finite element method. Hence, a thermal analysis of the numerical model is performed, and the calculated temperature field is subsequently subjected to thermo-mechanical analysis. In the latter model, the two defects located in the most critical position, detected experimentally by performing fatigue tests on the same component, are introduced into the model by using the constrained crack faces technique. Furthermore, to enable the thermo-mechanical simulation of the FSW process, temperature-dependent non-linear material properties, material softening, and isotropic hardening are considered. Concerning fatigue crack growth analysis, three simulations of the fatigue crack propagation are performed by using three different propagation laws. The first is performed by considering linear elastic material properties and Vasudevan's law on fatigue crack propagation; the second is by employing non-linear material properties and Kujawski–Ellyin law; the third takes into account the non-linear material properties and UniGrow law. Thereafter, appropriate constraints and a remote fatigue load are applied to the specimen to allow residual stress redistribution and fatigue crack growth, respectively. The constraint effect is also evaluated by the calculation of the T-stress parameter. Finally, a comparison between the numerical and experimental results is presented; consequently, a better agreement with the case of the non-linear model under the SSY conditions is found.

1. Introduction

Fatigue crack propagation in structural components has always been a difficult problem in several critical applications [1,2]. For instance, it is well-known that residual stresses that are induced at the manufacturing and welding stage assume a key function in crack growth assessment [3,4]. Friction stir welding (FSW) is a related new solid-state welding technology whose application to aluminium structures is significantly increasing. Relevant benefits that are achievable by the FSW process, with respect to conventional fusion welding techniques, are related to reduced porosity, distortion, and residual stresses. In recent years, several studies

* Corresponding author.
E-mail address: malepore@unisa.it (M. Lepore).

Nomenclature

A, B	surface break-through points
A, o, m	Vasudevan's law parameters
A_k, B_k	Nasgro coefficients
b	fatigue strength exponent
B^*	plane stress or plane strain selection
C	middle position break-through point
C^*	UniGrow constant
c	fatigue ductility exponent
c_p	specific heat capacity
CCFT	constrained crack faces technique
da_{max}	maximum advancing crack increment
dN_{low}	minimum dN value
E	Young modulus
EPFM	elastic-plastic fracture mechanics
ERR	energy release rate
FCG	fatigue crack growth
f_{conv}	conversion factor of ERR
FEM	finite element method
FPZ	fracture process zone
FSW	friction stir welding
G^*	shear modulus
G_{eq}	equivalent energy release rate
$G_{max,eq}$	maximum of the equivalent energy release rate
I_n	constant of HRR stress-strain field
J_1, J_2, J_3	J-integral terms of modes I, II, and III
K	thermal conductivity
KE	Kujawski–Ellyin
K_I, K_{II}, K_{III}	stress intensity factor of modes I, II and III
K_C	fracture toughness
K_{IC}	mode I fracture toughness
K_{max}	maximum value of stress intensity factor
$K_{max,th}$	fatigue threshold of K_{max}
K_{min}	minimum value of stress intensity factor
LCF	low-cycle fatigue
LEFM	linear elastic fracture mechanics
MERR	maximum energy release rate
n	strain hardening exponent
$\bar{n}$	strain energy density ratio
n	number of tool revolutions per minute
n'	cyclic hardening exponent
p	UniGrow exponent
p_k	components of volume forces
q	surface heat flux
$\dot{Q}_{gen}$	volumetric heat source term
R	stress ratio
R_s	stress ratio-dependent regions I, II, and III
R'	correction factor of R
r,θ	polar coordinates of HRR field
r'	radial position originating from tool centre
r_c	radius of cyclic plastic zone
r_m	radius of monotonic plastic zone
RKE	Rice, Kujawski, and Ellyin stress-strain field
SIF	stress intensity factor
SWT	Smith Watson Topper
T	temperature
t_0	plate thickness
UniGrow	unified two-parameter fatigue crack growth driving force
VCE	virtual crack extension
W(ε)	strain energy density
W(σ)	complementary strain energy density
W^e	elastic strain energy density
W^p	plastic strain energy density
x	distance from the crack tip
$\bar{x}$	reduction in area
α	material parameter
β	Coffin–Manson exponent
γ	UniGrow exponent
δ^*	length of fracture process zone
ζ	term to select plane stress or plane strain condition
$\Psi_{y,1}$	averaging constant corresponding to the ith elementary block
υ	Poisson's ratio
ρ	material density
ρ^*	length of crack extension
ρ_c	crack-blunting radius
σ_{yield}	temperature-dependent yield stress
σ_{ij}	components of stress tensor
σ_m^*	local mean stress
σ_y'	fatigue strength coefficient
σ_u	ultimate strength
e_{ij}	known dimensionless function of hardening exponent n
ϵ_f'	fatigue ductility coefficient
ε_{ij}	components of strain tensor
ε_{ij}	known dimensionless function of hardening exponent n
ΔK	stress intensity factor range
ΔK_{th}	threshold value of stress intensity factor range
$\Delta K_{max,th}$	maximum value of fatigue threshold
ΔK_{tot}	total stress intensity factor range
Δκ	unified two-parameter fatigue crack growth driving force
Δ√G	energy release rate factor range

have been implemented to develop numerical tools that are capable of predicting the fatigue behaviour of welded structures [5–14]. Furthermore, some recent contributions have been published in the literature dealing with the numerical determination of residual stress fields and the analysis of their combination with stress fields including their effects under loading [15,16]. Regarding the FSW, the established models for residual stress evaluation, such as that proposed by Hattel et al. [21], can be found [17–20]. Comprehensive review articles concerning the FSW modelling and stress analysis are available in Refs. [22,23].

As for the fatigue crack propagation, in this work, a realistic prevision of the propagation life of a friction stir-welded sample is presented by employing the small-scale yielding (SSY) condition. However, the simulation of the fatigue crack propagation is also performed using the linear elastic fracture mechanics (LEFM) approach. The advantage of the LEFM results from the linearity of constitutive equations and assumption of small strains; consequently, closed form solutions for stress and strain fields at a crack tip can be obtained. This is generally not possible in incremental plasticity, as the constitutive equations are non-linear, and the current stress-strain state depends on the loading history. By employing an approach based on the deformation theory of plasticity and the

introduction of 'path-independent integral' by Cherepanov [57] and Rice [58], a perfect analogy of the LEFM could be established in elastic-plastic fracture mechanics (EPFM) [59]. The J-integral is regarded as an intensity parameter of the crack-tip fields and a plastic energy release rate [59]. The determination of the J-integral in finite element (FE) codes is based on the domain integral method in contour integral evaluation [59], which was first suggested by Parks [60,61] and further developed by DeLorenzi [62,63]. The method is considerably robust, and accurate values are obtained even by employing relatively coarse meshes [64]. Because the domain integral is based on energy quantities and is applied over a finite region of elements, the effect of stress discontinuities or any other numerical imprecisions of local field quantities is minor [59]. Furthermore, the J-integral is defined in terms of the energy release rate associated with a fictitious small crack advance. Because of this interpretation, the domain integral method is also known as the 'virtual crack extension' (VCE) method [59].

In the EPFM, the Hutchinson–Rice–Rosengren (HRR) singularity is considered; however, special crack tip elements for modelling this singularity are yet to be established. In the adopted tool for fracture mechanics, Zencrack, 'retained' the tip elements that are available. They are similar to collapsed elements, but with unchanged midside nodes (a 20-node hexahedral element). Considering a hexahedral eight-node element, a midside dummy node is automatically set by the Zencrack code [25]; accordingly, an ideal plastic 1/r singularity in the strains results. Moreover, considering that AA2024-T3 exhibits a hardening exponent $n > 10$, the asymptotic behaviour approaches ideal plastic equations [65].

Hutchinson [68] and Hilton and Hutchinson [67] were among the first to consider the existence of plastic stress intensity factors under the conditions of small and large-scale yielding, respectively. They have shown that the plastic stress intensity factor in small scale yielding can be directly related to elastic stress intensity factors, and the use of plastic intensity factors is in no way restricted by the extent of the plastic zone [68]. Rice, instead of emphasising plastic intensity factors, uses the value of a path-independent integral, which is defined in the deformation theory as a measure of the level of deformation at the crack tip. It is noteworthy that these approaches lead to identical results as long as the deformation theory of plasticity is employed [67]. Moreover, it has been shown by Hilton and Sih [70] that even though the elastic–plastic boundary has been considerably distorted from that associated with the SSY conditions at half the yield stress, the plastic stress intensity factor (SIF) still yields accurate predictions for fracture initiations at this level of applied stress [66,69]. Consequently, if the plastic energy release rate is considered, then it is possible to describe the stress–strain behaviour ahead of the crack front under the condition of both small and large-scale yielding. However, to avoid confusion on the theoretical assumptions on which this work is based, recall that the LEFM is based on the assumption of the SSY, which can also be considered as the basic reference for non-linear fracture mechanics [71]. Considering Irwin's theory, in which a fictitious extension of the crack was presented in order to calculate the size of the plastic zone, an effective crack length, a_{eff}, is obtained corresponding to an effective SIF, K_{eff}. Under these conditions, an 'effective' energy release rate for the SSY can be written as follows: $G_{SSY} \approx G^e + G^p$ [59].

Thus, the stress intensity factor range, ΔK, expressed by models proposed for the SSY, is equivalent to an elastic-plastic term [59] obtained by the conversion of the effective energy release rate, $\Delta\sqrt{G}$, via a conversion factor [59].

The finite element method (FEM)-based procedure is proposed and tested to simulate the fatigue propagation of two three-dimensional (3D) cracks in a friction stir welded sample, using both the LEFM and SSY conditions. In considering the cracks in three-dimensional components, the nominal applied fracture mode could induce coupled modes close to free surfaces because of three-dimensional effects; these have been discussed in the pioneering contributions of Bažant and in more recent contributions of Pook et al. [28–31]. Furthermore, considering that the residual stress field is three-dimensional, an equivalent range of the SIF has been adopted in fatigue crack propagation laws. Finally, both the Kujawski–Ellyin (KE) and UniGrow approaches are based on the concept of the fracture process zone (FPZ). A small region ahead of the crack front, where the process of stable growth is basically associated with yielding, is called the 'plastic zone' [32]. The KE model considers that such plastic region is smaller than the cyclic plastic zone. Otherwise, the UniGrow model, in the form proposed by the authors, considers a process zone that corresponds to the whole cyclic plastic zone. Thus, if the fatigue load is sufficiently low, then a small deformation in the region ahead of the crack front is achieved; thereafter, these two models tend to predict the same number of cycles.

2. Materials and methods

In this section, the approach developed in the present work is described. An uncracked FEM model is used to obtain a residual stress distribution by a thermo-mechanical simulation of the welding process. More precisely, two cracks are introduced at the selected locations of the domain before the thermo-mechanical simulation is run using the constrained crack faces technique (CCFT). In this case, such defects cannot be considered as 'cracks' as a result of enforcing material continuity through the application of contact constraints; these prevent the interpenetration as well as the mutual displacement of crack faces [34]. In this way, the 'cracked' FE model is considered equivalent to the uncracked model. Furthermore, before the simulation of the fatigue crack growth is run, such contact constraints are removed; this allows the residual stresses to redistribute, which leads to a new equilibrium condition. In other words, the contact constraints imposed on the crack faces are first removed. Thereafter, a fatigue load is applied to one end of the specimen, whereas some constrains prevent displacements along the three directions of the global reference system on the other end [34] (Fig. 8). For optimising accuracy, the crack growth simulation is divided into two distinct steps. The first step spans until the central crack becomes a through-thickness crack; that is, when only two crack fronts are present in the model. The second step is initiated when the central crack becomes a through-thickness crack. It spans until the number of cycles provided by the experimental test for the lateral crack is matched; that is, when the central crack is subdivided into two new fronts. Thereafter, three crack fronts are considered in the model. Thus, two crack growth simulations are performed using the KE model [26] and the unified two-parameter fatigue crack growth driving force (UniGrow) model [27]. For both implemented models, a non-linear material

behaviour is considered. In the numerical simulation under the condition of the SSY, the non-linear material behaviour, as well as crack-blunting, is taken into account [25]. Hence, the procedure has implemented three consecutive steps that aim at the creation of the finite element model, the simulation of the welding process (i.e., the definition of the residual stress scenario), and the crack propagation simulation. These steps are named as pre-welding, welding simulation, and crack propagation, respectively (Fig. 1). Each step is detailed in the following section.

2.1. Pre-welding

First, the geometric model is meshed without modelling the cracks. Subsequently, a thermal analysis is performed in order to obtain a temperature distribution throughout the domain [11]. Afterwards, the commercial code, Zencrack [25], is allowed to introduce two cracks into the model; this locally changes the mesh. Thereafter, the constrained crack faces technique (CCFT) is used [34]. Contact constraints are imposed on the crack faces in order to prevent their separation or any related node movement. Such constraints prevent the interpenetration of crack faces as well as related movements in the normal and tangential directions. In particular, the double crack nodes that do not belong to the front line are fully constrained; in this way the same displacement and stress values are imposed. Accordingly, this model can be considered as uncracked; it is prepared for the next crack opening by simply releasing the aforementioned pre-imposed conditions.

2.2. Welding process

The friction stir welding process, which is used as a benchmark in the present study, has been extensively investigated by several authors [35,36]. Two AA2024-T3 plates are joined to create a butt weldment according to the dimensions indicated in Fig. 2. The experimental test features a steel tool with a flat shoulder (20 mm in diameter) and a smooth pin (the larger diameter is 6.2 mm, 30° cone angle, and 3.8-mm height) rotated at a speed of 1400 rpm, with a welding speed of 70 mm/min and a tilt angle of 2°. The rotational and translational movements of the tool along the welding path generate frictional heating of the underlying components and intimately remix the base material; this also leads to the formation of microstructurally different zones [37]. The chemical composition and the main mechanical characteristics of the considered alloy are well-known and available in the literature [9]. The residual stress distribution that is generated by the welding process is numerically evaluated by the thermo-mechanical model designed and validated by Hattel et al. [38,39]. In this model, the two starting plates are considered as a single body with uniform material properties throughout the domain. Hence, the contact between the rotating pin and plate is modelled; however, a heat flux, which moves along the welding line, is simulated. Moreover, the softening and hardening behaviour of the material, which is generated by the thermal flux in the weld bead, is simulated. For completeness, the fundamentals of this model are herein reported. An exhaustive description of the thermo-mechanical model is available in Ref. [11].

The lateral crack is introduced in the FE model at 97 mm from the bottom surface, whereas the central crack is positioned at 87 mm from the same reference surface. In addition, the lateral crack is a rectangular through-thickness crack with its shorter side measuring 2.5 mm. The central crack is a semi-elliptical surface crack that measures 1.9 mm along the lower semi-axis and 5.6 mm along the longer one. The spring (shown in green in Fig. 3) values applied here are equal to 2.0E6 and 4.0E3 N/mm along the Z and Y directions, respectively. To introduce these springs on the external surfaces of the crack blocks [25], a .input file has been written for the lateral crack and called by ABAQUS when it runs the main .inp file. The nodal constraints (shown in orange in Fig. 3) are both

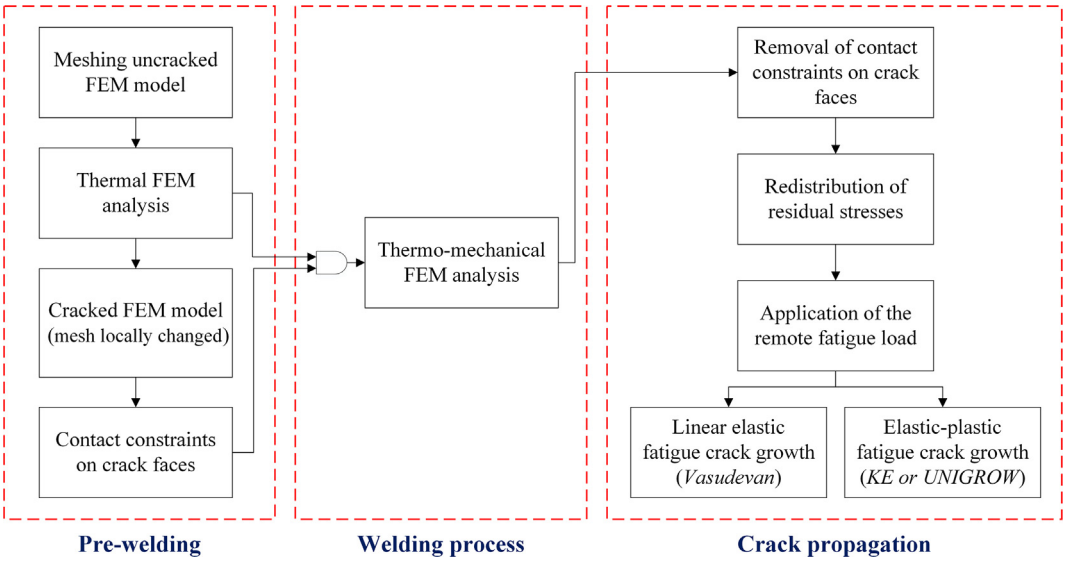

Fig. 1. Flowchart of adopted procedure.

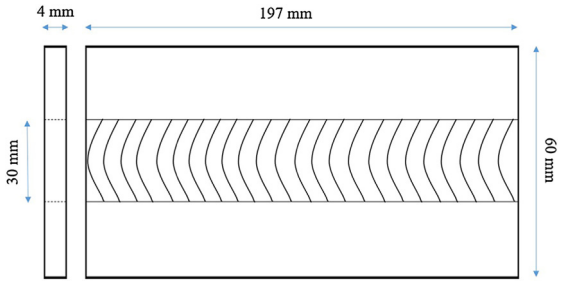

Fig. 2. Model geometry and dimensions.

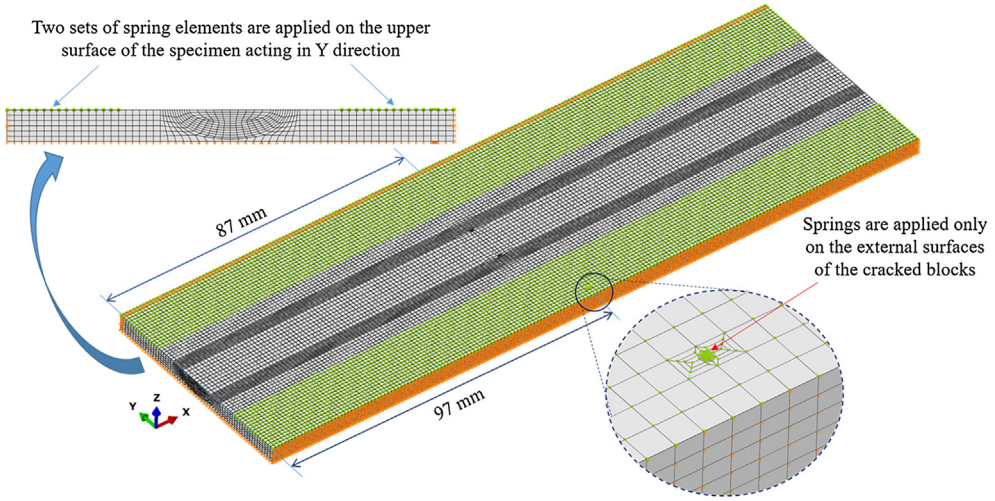

Fig. 3. FE model highlighting the region containing the lateral crack and boundary conditions details.

applied on the bottom and lateral surfaces. The constraints applied on the bottom surface of the specimen are directed along the Z direction, whereas the constraints applied on the lateral surfaces are directed along the Y direction; such constraints prevent any displacements in the Y and Z directions. In the other three nodes, each of which is located at the three ends of the plate and at the middle of the thickness, the constraints prevent the displacement along the X direction [34].

The model is based on the commonly accepted assumption that disregards the material flow [19] because it reduces the computational complexity of simulation without penalising the accuracy in the final assessment. With that hypothesis, the thermo-mechanical problem reverts back to a Lagrangian form that makes it possible to calculate the entire solution of the problem into two distinct moments: thermal and mechanical; the two are solved sequentially. In particular, the latter is solved after importing the transient temperature distribution deduced by thermal analysis. The time-dependent temperature distribution is obtained by solving the equation of transient heat conduction written as

$$\rho c_p \frac{\partial T}{\partial t} = \frac{\partial T}{\partial X}\left(k\frac{\partial T}{\partial X}\right) + \frac{\partial T}{\partial Y}\left(k\frac{\partial T}{\partial Y}\right) + \frac{\partial T}{\partial Z}\left(k\frac{\partial T}{\partial Z}\right) + \dot{Q}_{gen} \tag{1}$$

where c_p is the specific heat capacity, T is the temperature, k is the thermal conductivity, and $\dot{Q}_{gen}$ is the volumetric heat source term. The tool action is simulated through an appropriate boundary condition that applies to the interface between the shoulder and specimen. A radial and superficial heat flow, q, which depends on the tool position and local yield stress (a function of temperature), is imposed on the contact area between the tool and material without the necessity of modelling the probe [36], as the following:

$$q(r', T) = (2\pi n/60) r' \frac{\sigma_{yield}}{\sqrt{3}} \tag{2}$$

where q is the surface heat flux, n is the number of tool revolutions per minute, r' is the radial position originating from the tool centre, and σ_{yield} is the temperature-dependent yield stress. Furthermore, this stress is regulated by a series of steps to allow the material softening to be attributable to microstructural changes. Essentially, the yield stress is adjusted at each step because of the dissolution of a hardened precipitate caused by heating. For this purpose, the model of Myhr and Grong [39] is adopted, as suggested in Ref. [13].

The equilibrium equation, solved by mechanical iteration, is given by the following:

$$\sigma_{ij,k} + p_k = 0 \tag{3}$$

In Eq. (3), $\sigma_{ij,k}$ and p_k are the components of stress tensor and volume forces, respectively. The previously evaluated temperature distribution is used to calculate the thermal strain, which is applied as an internal load in the mechanical model. Together with the expression for thermal deformation, an implicit numerical scheme that is based on the adoption of the generalised Hooke law and linear decomposition of the strain tensor is applied. The standard flow theory (J_2) with the von Mises yielding surface, which is dependent on temperature and isotropic hardening, is used to evaluate the development of plastic strains [36]. The ABAQUS software is used to implement and solve the thermo-mechanical model. A validation of the model with respect to temperature and stress calculation for the considered benchmark can be found in Refs. [20,21]. The material properties that are used for simulating the thermal softening are summarised in Table 1.

The simulation of the thermo-mechanical problem consists of a sequence of five calculation steps. In the initial step (Initial), a uniform temperature of 25 °C is introduced to the entire domain. In the second (HeatIni), a heat source is generated. In the third step (HeatMove), the heat source is translated along the welding path (X axis of the global reference system shown in Fig. 2); this simulates the creation of the weld bead. In the fourth (CoolDown), joint cooling is achieved until the initial temperature is reached. In the fifth step (Releasing), the initial boundary conditions are removed and new boundary conditions are introduced to eliminate only the degrees of freedom of rigid body. At the end of the latter step, the field of residual stresses is produced. The mesh of the uncracked model consists of 11 956 hexahedral elements (C3D8 and SPRING1), which corresponds to 114 793 nodes, and its thickness is modelled with a row of six hexahedral elements. Moreover, because the lateral crack is a through-thickness crack. Each element of the uncracked model positioned along the direction of the development of the crack front and of each crack side is replaced by a crack block obtained from a library [25]. In this case, the standard block that belongs to the S04 family is used [25]. Hence, the same type of crack block is used to model the central crack.

2.3. Crack propagation

After residual stresses are calculated, the constraints imposed on the crack faces are removed and allows the cracks to open. In this way, the residual stresses can be redistributed before the start of the simulation of the crack propagation; in particular, such a redistribution involves the whole domain. Thereafter, the fatigue load is applied on the specimen, and the crack growth simulation, driven by a suitable propagation law, is initiated; both linear elastic and non-linear material behaviours are considered. Regarding the lone non-linear case, the simulation of the fatigue crack propagation can be divided into two different sub-steps. The first is related to the crack propagation that stops when the central crack becomes through-thickness; the second is related to the crack propagation when the central crack becomes a through-thickness crack. In the latter case, the central crack is divided into two new crack fronts. Hence, a few other crack propagation steps are implemented to achieve the final number of cycles established by the experimental test. It is remarkable that the non-linear behaviour of AA2024-T3 is modelled according to the Ramberg–Osgood equation [33]. The values of the true stress–strain curve for AA2024-T3 are reported in Fig. 4 [40].

The same model geometry that is used for calculating the residual stress field is employed for the simulation of fatigue crack propagation. Some constraints, directed along the X, Y, and Z axes of the global reference system, are applied to one end of the joint; at the other end, a uniform remote stress (100 MPa), directed along the X axis, is applied [34]. Furthermore, at the beginning of the simulation, an initial temperature of 25 °C is set on the whole domain according to the experimental test [34].

2.4. Methods for calculating fracture parameters

The interaction between Zencrack and ABAQUS allows the insertion of cracks with the simultaneous replacement of initial hexahedral elements, which contain a part of the crack front with crack blocks [25]. This implies an adaptation of the surrounding mesh that is produced through controlled and gradual deformations of neighbouring elements. Through Zencrack, a propagation law is inserted, as well as crack growth and post-processing of fracture parameters from calculations. It is noteworthy that crack modelling is only possible if the mesh of the starting model (uncracked) is made of hexahedral elements [25]. Each crack is defined by a set of collapsed blocks that are classified into two groups: the first, which consists of collapsed facing elements obtained from a library

Table 1
Material properties for thermal softening.

Yield stress (MPa)	Strain	Temperature (°C)
306	0	20
501	0.1	20
261	0	100
456	0.1	100
152	0	200
317	0.1	200
57	0	300
87	0.1	300
13	0	400
28	0.1	400
5	0	500
10	0.1	500

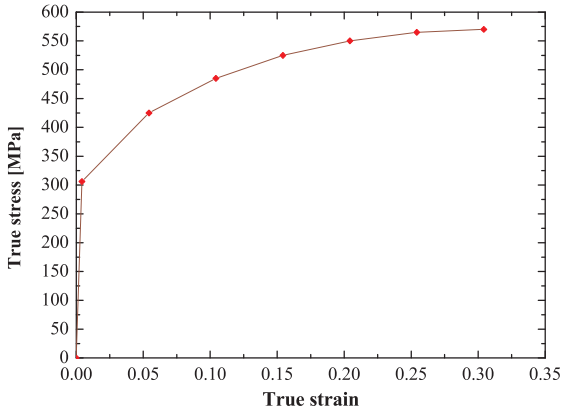

Fig. 4. Experimental data used to model a Ramberg–Osgood material behaviour.

where they are stored in families, is used to model the crack front; the second consists of pairs of facing blocks, whose adjacent nodes are separated and used for modelling the crack faces. Each crack block is a set of 3D elements positioned inside a cube, each of which contains only a part of the crack front; therefore, each face can be modelled with only one block or multiple adjacent blocks depending on the crack extension. In the crack block library, two macro families of crack blocks are identified: the first, contains 'standard' blocks; the second, contains 'large' blocks. In this work, the FE simulations use 'standard' blocks [25].

Based on the selected criterion for defining the direction of the fatigue crack propagation, the maximum energy release rate (MERR) is used for kink angle estimation. Zencrack is used to exploit the virtual crack extension (VCE) technique, which is available in ABAQUS, to generate multiple virtual crack extension vectors. In cases of tridimensional defects, it is possible to define a normal plane to the crack front, in which up to seven vectors originate from the considered node of the front. The angles, defined by each vector with the local plane of the crack to be extended, differ among each other; the angles also determine a computing position for the energy release rate (ERR). Among these calculated values of the ERR, one is maximum [25]. Then, the angle formed between the plane of the initial crack to be extended and the vector at which the ERR is maximum (MERR) becomes a propagation 'direction' for that node. This technique is repeated for each node of the crack front; accordingly, it allows obtaining a realistic engineering front in which each node is associated with a kink angle.

The predictive method used to extend the crack is the 'forward predictor'. At each front node, a maximum user-defined 'da_{max}' advancing crack increment is applied and introduced into the adopted propagation law. After the integration of such law, dN values are obtained in each node of the front. Thereafter, between these calculated values, the minimum dN value (dNlow) is detected and applied to all nodes of the crack front. Finally, a new integration is made for each node with an assumed constant ratio (dG/da) along the current crack increment (forward predictor). The current 'da' value is recalculated at each point of the front; this corresponds to a cycle number, dN_{low}.

2.5. Propagation laws

2.5.1. Linear model: Vasudevan's law

The contour method is used by ABAQUS to calculate J-integral values, which are subsequently converted by Zencrack into stress intensity factors (SIFs) and provided as inputs to the adopted propagation law. The residual stresses affect the crack growth as they change the total value of the calculated SIF along the crack front. These stresses simultaneously act on the minimum (K_{min}) and maximum (K_{max}) K, but leaves $\Delta K = K_{max} - K_{min}$ unaltered. With the Vasudevan model [41], the main effect of the residual stresses on the crack growth rate is considered related to the variations of K_{max} rather than ΔK. Considering a two-parameter model (Vasudevan), the fatigue propagation of the crack is driven by two forces—ΔK and K_{max}; hence, residual stresses can affect the growth rate although they do not affect ΔK. Moreover, this theory considers two fatigue threshold values: $K_{max,th}$ and ΔK_{th}, which correspond to the K_{max} and ΔK driving forces. Such forces must be greater than the threshold values because the fatigue crack propagates. Because residual stresses affect K_{max} levels, a propagation may stop if the stresses are compressive and have a value such that K_{max} is less than $K_{max,th}$. The law is represented as follows:

$$da/dN = A(\Delta K - \Delta K_{th})^{o}(K_{max} - K_{max,th})^{m} \tag{4}$$

The crack growth law is calibrated using only experimental data from a constant amplitude test. The experimental threshold data and

Table 2
Propagation law parameters.

ΔK_{th} (N/mm$^{3/2}$)	$K_{max,th}$ (N/mm$^{3/2}$)	A (mm$^{1.5(n+m)+1}$/N^{n+m})	o	m
52	106	5.9427E−10	1.65	0.56

material parameters (A, o, m) are obtained from the literature [9,42], as summarised in Table 2. Thereafter, da/dN is expressed in mm/cycle and ΔK in $N/mm^{3/2}$. Such values are valid for every positive R-ratio [9] (in this work R = 0.1). The residual stress effects are evaluated by considering the crack growth law (Eq. (4)). In this law, the SIF is defined by the sum of the nominal SIF, corresponding to the remote load, plus the SIF, corresponding to the contribution of the residual stresses induced by the FSW.

In addition to the parameters listed in Table 2, K_c within the fatigue crack propagation for a minimum constraint condition is computed with the following expression:

$$K_c = (1 + e^{-(t/t_0)})K_{Ic} = (1 + 0.84)1008 \ \ \text{MPa}\sqrt{\text{mm}} = 1856 \ \ \text{MPa}\sqrt{\text{mm}} \tag{5}$$

where $t_0 = 2.5(K_{Ic}/\sigma_y)^2 = 2.5(1008/331)^2 = 23.18$ mm, t = 4 mm is the plate thickness, $K_{Ic} = 1008$ MPa $mm^{0.5}$ is the plane strain fracture toughness, $A_k = 1.0$, $B_k = 1.0$, and $\sigma_y = 331$ MPa. These data are derived from the NASGRO [43] database for Al 2024-T3 Clad & Bare Sht and T-L; LA & HHA [M2EA12AB1], which is the particular material that enhances the approaches used herein. The details are as follows: Clad & Bare Sht = sheet with treated and untreated surface; T-L = transverse–longitudinal specimen crack orientation; LA = laboratory or 50% relative humidity air; HHA = high humidity air; M2EA12AB1 = NASGRO material code [44]. In addition to K_I, K_{II}, and K_{III}, the parameters ΔK and K_{max}, which are used in Vasudevan's formula, also consider the following quantities:

$$\Delta K_{eq} = \{E/[1 - (\zeta\upsilon)^2]\}^{1/2}\Delta\sqrt{J_{eq}} \tag{6}$$

$$K_{max,eq} = \{E/[1 - (\zeta\upsilon)^2]\}^{1/2}\sqrt{J_{max,eq}} \tag{7}$$

then:

$$J_{eq} = \frac{B^*}{E}(K_I^2 + K_{II}^2) + \frac{1}{2G^*}K_{III}^2 \tag{8}$$

where $B^* = (1 - (\zeta\upsilon)^2)$ for plane strain, $B^* = 1$ for plane stress, and G^* is the shear modulus;

$$J_{max,eq} = J_{1,max} + J_{2,max} + J_{3,max} \tag{9}$$

However, the K_{II} and K_{III} values calculated along the crack fronts are negligible in this case; accordingly, the propagation is dominated only by mode I. It is noteworthy that the propagation law used in this work is written in terms of the stress intensity factor (K). Zencrack calculates energy release rate (ERR) and completely converts values to K (K conversion) automatically in each calculation step.

Alternatively, because propagation transpires in pure mode I, it is possible to rewrite Vasudevan's proposed law in energys terms by considering Δ ($J^{1/2}$) instead of ΔK; $(J_{max})^{1/2}$ and $(J_{min})^{1/2}$ instead of K_{max} and K_{min}, respectively.

Therefore, it is possible to write ΔJ_{th} as

$$\Delta J_{th} = \Delta K_{th}^2[1 - (\zeta\upsilon)^2]/E \tag{10}$$

and then to rewrite ΔK_{th} as

$$\Delta K_{th} = \Delta J_{th}^{1/2}[E/(1 - (\zeta\upsilon)^2)]^{1/2} \tag{11}$$

where ζ is a measure of the stress triaxiality degree, which may vary between 0 and 1 (ζ = 0 for plane stress and ζ = 1 for plane strain condition), and υ is Poisson's ratio. The same is true for $K_{max,th}$; accordingly, it can be rewritten as

$$J_{max,th} = \{K_{max,th}^2[1 - (\zeta\upsilon)^2]\}/E \tag{12}$$

$$\text{andthen} \ \ K_{max,th} = J_{max,th}^{1/2}\{E/[1 - (\zeta\upsilon)^2]\}^{1/2} \tag{13}$$

Finally, the stress ratio R can be written as

$$R = \frac{J_{min}^{\frac{1}{2}}}{J_{max}^{\frac{1}{2}}}, \ \ \text{and Vasudevan's law can be rewritten as} \tag{14}$$

$$\frac{da}{dN} = A\left[\frac{E}{1 - (\varsigma\nu)^2}\right]^{(o+m)/2}(\Delta\sqrt{J_{eq}} - \Delta\sqrt{J_{th}})^o(\sqrt{J_{max,eq}} - \sqrt{J_{max,th}})^m \tag{15}$$

2.5.2. Non-linear model: The Kujawsky–Ellyin law

For a strain-hardening material that obeys the Ramberg–Osgood law, the monotonic solution for the elastic–plastic field ahead of a crack tip given by Hutchinson, Rice, and Rosengren, is commonly known as the HRR singularity field [45].

In this case, the stress and strain fields are expressed as follows:

$$\varepsilon_{ij} = \sigma_0/E\{[EJ/(\alpha I_n\sigma_0^2 r)]^{n/(1+n)}e_{ij}(n, \theta) + \alpha[EJ/(\alpha I_n\sigma_0^2 r)]^{1+(1+n)}\varepsilon_{ij}(n, \theta)\} \tag{16}$$

$$\sigma_{ij} = \sigma_0[EJ/(\alpha I_n\sigma_0^2 r)]^{n/(1+n)}\sigma_{ij}(n, \theta) \tag{17}$$

where r and θ are polar coordinates, andε_{ij}, e_{ij}, and σ_{ij} are known as dimensionless functions of θ and strain-hardening exponent, n; I_n is a constant dependent on n and stress state (i.e., plane stress or plane strain), whereas, J is a path-independent integral, and σ_0 is an effective yield stress. Starting from the previous formulas (16) and (17) of stresses and strains, a tensile loaded crack (Mode I) within the monotonic plastic zone can be found by applying the Kujawski and Ellyin method [32] based on an energy interpretation of the strain-hardening exponent (n). Furthermore, from the hypothesis of small scale yielding and plane stress condition ($K^2 = EJ$), and considering a two-dimensional crack front, the stress and strain components normal to the crack line can be written as [45] follows:

$$\varepsilon(x, 0) = \sigma_0/E\{K^2/[(1 + \bar{n})\pi\sigma_0^2 x]\}^{\bar{n}/(1+\bar{n})} + \sigma_0/E\{K^2/[(1 + \bar{n})\pi\sigma_0^2 x]\}^{1/(1+\bar{n})} \tag{18}$$

$$\sigma(x, 0) = \sigma_0\{K^2/[(1 + \bar{n})\pi\sigma_0^2 x]\}^{\bar{n}/(1+\bar{n})}$$

The expressions in Eq. (18) are commonly referred to as the RKE (Rice–Kujawski–Ellyin) fields,

$$\text{where } \bar{n} = W(\sigma)/W(\varepsilon) = \left[1 + n\left(\frac{W^p}{W^e}\right)\right]/\left[1 + \left(\frac{W^p}{W^e}\right)\right] \tag{19}$$

$$W(\varepsilon) = \int_0^{\varepsilon} \sigma d\varepsilon \text{ is the strain energy density,} \tag{20}$$

$$W(\sigma) = \int_0^{\sigma} \varepsilon d\sigma \text{ is the complementary strain energy density,} \tag{21}$$

$$W^e = \frac{\sigma^2}{2E} \text{ and } W^p = \left[\frac{1}{(1 + n)}\right]\sigma\varepsilon^p \tag{22}$$

are the elastic and plastic components of strain energy density, respectively.

Considering the monotonic plastic zone, the maximum cyclic stress and strain components normal to the plane of crack growth within the plastic zone can be written as follows:

$$\sigma_{max} = \sigma_0\{K_{max}^2/[(1 + \bar{n})\pi\sigma_0^2 x]\}^{\bar{n}/(1+\bar{n})} \tag{23}$$

$$\varepsilon_{max} = \varepsilon_0\{K_{max}^2/[(1 + \bar{n})\pi\sigma_0^2 x]\}^{1/(1+\bar{n})} \tag{24}$$

where $\sigma_0 = E\varepsilon_0$ is the tensile yield stress, $\bar{n}$ is the ratio used in Eq. (19), and x is the distance from the crack tip. If the cyclic plastic zone is to be considered, then it is necessary to take into account low-cycle fatigue (LCF) properties; thereafter, the maximum cyclic stress and strain components normal to the plane of the crack growth within the cyclic plastic zone can be written as follows:

$$\sigma_{max} = \sigma_y'\{K_{max}^2/[(1 + \bar{n}')\pi\sigma_y'\delta^*]\}^{\bar{n}'/(1+\bar{n}')} \tag{25}$$

$$\varepsilon_{max} = \varepsilon_y'\{K_{max}^2/[(1 + \bar{n}')\pi\sigma_y'\delta^*]\}^{1/(1+\bar{n}')}$$

where σ_y' is the cyclic yield strength; $\bar{n}'$ is defined as that in Eq. (19) (however, instead of n, the cyclic hardening exponent n' is used); δ^* is a length in the crack extension direction, called 'fracture process zone' (FPZ), in which the majority of the damage is experienced by the material. However, in this work, $\bar{n}' = n'$ is employed as suggested in Ref. [46]. In the KE model, δ^* is written as

$$\delta^* = \Delta K_{th}^2/[4\pi E\varepsilon_f'(1 + n')(\sigma_f' - \sigma_m)] \tag{26}$$

thereafter, this value is assumed to be a constant that represents a material length parameter [46]. In this work, another expression for δ^* is used [47] and shown in Eq. (27):

$$\delta^* = (\Delta K^2 - \Delta K_{th}^2)/\pi E\sigma_y' \tag{27}$$

where δ^* is a parameter that depends on the driving force of the stress–strain field, ΔK.

To account for crack-blunting effects, a critical crack-blunting radius, ρ_c, which is associated with ΔK_{th}, is introduced. Thereafter, in Eq. (26), the δ^* terms should be replaced with the parameter ($\delta^* + \rho_c$). However, ρ_c can be expressed even according to the concept of crack opening displacement [47]; specifically,

$$\rho_c = \Delta K_{th}^2/(\pi E\sigma_y') \tag{28}$$

$$\text{or, alternatively, as } \rho_c = \{1/[4\pi(1 + n')]\}(\Delta K_{th}/\sigma_y')^2, \text{ as suggested in Ref. [48]} \tag{29}$$

The material and low-cycle fatigue properties are summarised in Table 3. Considering a stress ratio R = 0.1 [49],

Table 3
Material and LCF parameters (AA2024-T3).

ΔK_{th} (N/mm$^{3/2}$)	E (N/mm^2)	υ	σ_y' (N/mm^2)	σ_f' (N/mm^2)	ϵ_f'	n'	b	c
52	72 000	0.33	320	835	0.174	0.109	−0.096	−0.644

$$\sigma_y^{'} = (1 + \bar{x})\sigma_u\{-0.002/[log(1 - \bar{x})]\}^{0.16} \tag{30}$$

where σ_u is the ultimate strength; $\bar{x} = 0.203$ is the reduction in area (material reference: Boller and Seeger); E is Young modulus; υ is Poisson's ratio.

It has been explained that Zencrack calculates the ERR and makes a conversion to K. In the case of SSY, the conversion factor (f_{conv}) can be expressed using Eq. (31),

$$f_{conv} = \sqrt{E/(1 - \alpha\upsilon^2)} \tag{31}$$

where α describes the plane stress or plane strain condition [34], which is described in Eq. (8), and applied to Eq. (31), as shown in the following:

$$\Delta K = \Delta\sqrt{J}\cdot f_{conv} \tag{32}$$

Thereafter, the fatigue crack growth law [46], which is valid for the case of a non-linear material, can be rewritten as follows:

$$\frac{da}{dN} = 2\delta^*\{(\Delta K^2 - \Delta K_{th}^2)/[4(1 + n^{'})(\sigma_f^{'} - \sigma_m)\pi E\varepsilon_f^{'}\delta^*]\}^{1/\beta} \tag{33}$$

where $\beta = -(b + c)$, in which b and c are the fatigue strength exponent and the fatigue ductility exponent, respectively; $\sigma_f^{'}$ is the fatigue strength coefficient, and $\epsilon_f^{'}$ is the fatigue ductility coefficient. Moreover, it is noted in Eq. (33) that the proposed fatigue crack growth (FCG) law is based not only on the LCF parameters, but also on the effect of local mean stress. It can be written as,

$$\sigma_m = [(1 + R_s)/2]\sigma_{max} \tag{34}$$

It is noteworthy that σ_m changes within the plastic zone. More details are provided below. In Eq. (34), R_s is not generally coincident with the stress ratio, R, which comes from the remote tensile load. Three zones can be highlighted within the plastic zone as depicted in Fig. 5. Region I or the cyclic plastic zone, r_c, where plastic deformation occurs during the loading and unloading half-cycles. Region II is between the cyclic plastic zone, r_c, and the monotonic plastic zone, r_m. In Region III or the elastic zone after r_m, the cyclic strains are fully elastic during loading and unloading. The strain ratio, R, changes within the plastic zone, and it can be described using the equations shown below:

$$\text{if } \delta^* > r_m \Rightarrow R_s = R \tag{35}$$

$$\text{with } r_m = (1/2\pi)(\Delta\sqrt{J_{max}}\cdot f_{conv}/\sigma_y^{'})^2 \tag{36}$$

$$\text{if} r_c \le \delta^* \le r_m \Rightarrow R_s = R^{'} + [(log\delta^* - logr_c)/(logr_m - logr_c)](R - R^{'}) \tag{37}$$

$$\text{if}\delta^* < r_c \Rightarrow R_s = R^{'} - [(r_c - \delta^*)/r_c](1 - R^{'}) \tag{38}$$

$$\text{where } R^{'} = 1 - 2[(1 - R^2)/4]^{n^{'}/(1+n^{'})} \tag{39}$$

2.5.3. Non-linear model: The UniGrow law

The unified two-parameter fatigue crack growth driving force model (UniGrow) takes into account residual stress because of the application of a cycle load, and subsequently, the stress ratio effect on the fatigue crack growth. The driving force, Δκ, is expressed as a combination of the maximum SIF, K_{max}, and stress intensity range, ΔK, which is corrected for the presence of residual stresses. In its more general formulation, which accounts for the mean stress or the stress ratio effect on fatigue crack propagation, the deformation in the crack tip material is considered predominantly plastic. However, for the simulation of this study case, the adopted driving force formulation is described by considering a non-linear material behaviour subject to cyclic loading. Then, the UniGrow model is written

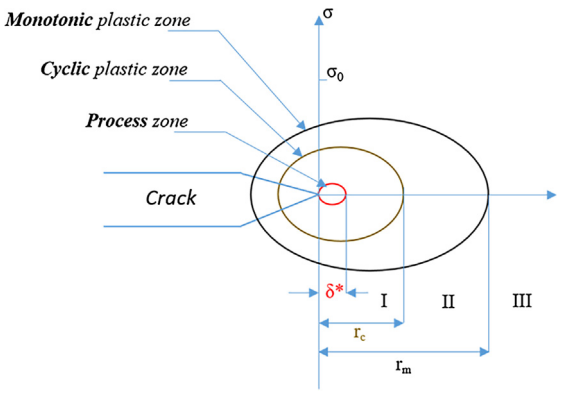

Fig. 5. Schematic of three regions within the plastic zone. Outside Region II the stress ratio is R = 0.1.

in a Fortran routine that is subsequently passed to Zencrack during the simulation.

Hence, in considering this approach, two main difficulties are found: the first is related to the determination of $K_{max,tot}$ and ΔK_{tot}, which requires substantial fatigue data [27]; the second is related to the determination of the elementary particle of finite dimension, ρ^*, i.e., of the process zone [27]. To solve the first problem, the solution provided by Huffman is adopted [50]. Hence, $K_{max,tot}$ and ΔK_{tot} are calculated with Eq. (40) because the residual stresses for the positive stress ratio can be taken into consideration using this equation:

$$K_{max,tot} = K_{max}\left[1 - \left(\frac{\sigma_{\varepsilon p=0.05} - \sigma_{\varepsilon p=0.001}}{\sigma_{\varepsilon p=0.05}}\right)(1 - R)\right] \tag{40}$$

where $\sigma_{\varepsilon p=0.05}$ is the stress at a plastic strain of 0.05, $\sigma_{\varepsilon p=0.001}$ is at a plastic strain of 0.001, and R is the stress ratio imposed on the fatigue test (R = 0.1). Thereafter, $K_{max,tot}$ is calculated with this formula, which shows that $K_{min,tot} = K_{min}$ because the minimum SIF is unaffected by the residual stresses; thus, it is equal to the applied K_{min} [27]. Using $K_{max,tot}$ and K_{min}, ΔK_{tot} is then calculated. The material and low-cycle fatigue properties as well as the cyclic yield strength are listed in detail in Table 2. Furthermore, $\Psi_{y,1}$ is the averaging constant corresponding to the ith elementary block [27].

Starting from the Paris law, the UniGrow model can be written as shown in the following:

$$da/dN = C^*(\Delta\kappa)^{\gamma} \tag{41}$$

where

$$\Delta\kappa = (K^{p}_{max,tot}\Delta K^{0.5}_{tot}) \tag{42}$$

$$\gamma = -1/b \tag{43}$$

$$C^* = 2\,\rho^*\left\{\frac{1}{2(\sigma'_f)^2}\left[\left(\frac{\psi_{y,1}}{\sqrt{2\pi\rho^*}}\right)^{3n'+1}(K'/E^{n'})\right]^{1/(n'+1)}\right\}^{-1/2b} \tag{44}$$

where $p = n'/(n' + 1)$ and $K' = \sigma'_f/\epsilon_f^{n'}$ is the cyclic strength coefficient obtained analytically.

Finally, the crack growth rate can be expressed in the form of Eq. (45), which is valid for a non-linear material, for which a stress ratio equal to R = 0.1 is considered.

$$\frac{da}{dN} = 2\rho^*\left\{\frac{1}{2(\sigma'_f)^2}\left[\left(\frac{\psi_{y,1}}{\sqrt{2\pi\rho^*}}\right)^{3n'+1}(K'/E^{n'})\right]^{1/(n'+1)}\right\}^{-1/2b}(K^{p}_{max,tot}\Delta K^{0.5}_{tot})^{\gamma} \tag{45}$$

Hence, ρ^* can be chosen using the average dimension of crack blocks surrounding the crack front [51] or using the following procedure. Three different equations that describe the cyclic plastic zone can be considered. Firstly, the use of the equation proposed by Antolovich–Saxena [52], which is valid for the plane strain condition and SSY hypothesis:

$$\rho^* = r_{pc} = const\,(\Delta K/\sigma_{ys})^2 \tag{46}$$

Thereafter, the equation suggested by Park et al. [53] is used:

$$\rho^* = r_{pc} = \frac{\pi}{144}(\Delta K/\sigma_{ys})^2 \tag{47}$$

where the first term of Eq. (46) has a *constant* value. Considering Eq. (48),

$$\rho^* = r_{pc} = r_c + \rho_c \tag{48}$$

where r_c and ρ_c are the plastic and the crack blunt radii, respectively, as proposed by Shi et al. [48].

Finally, based on the results of the three simulations obtained using each of the three different formulas for modelling the cyclic plastic zone, a convergence value of the *const* parameter can be found. In Eq. (49), the final expression of ρ^* described below, is used in this work.

$$\rho^* = r_{pc} = \frac{\pi}{24}(\Delta K_{tot}/\sigma_{ys})^2 \tag{49}$$

where r_{pc} is the radius of the cyclic plastic zone, σ_{ys} is the yield strength of the material, and ΔK_{tot} is obtained as the difference between $K_{max,tot}$ and K_{min} described previously. Eq. (49) is similar to the plastic zone size correction, r_y, proposed by Edmunds and Willis in Ref. [54], in which ΔK_{tot} is used instead of K_I. Moreover, in Eq. (49), σ_{ys} is used instead of σ_{yc} because ΔK_{tot} is expressed in the stress ratio R function, which depends on the monotonic load of Eq. (40). It is noteworthy that the fatigue crack propagation law of Eq. (45) is written by means of the Manson–Coffin equation in which the plastic term is omitted [51]. Furthermore, it should be noted that the driving force (Eq. (42)) directly results from the mean stress correction model, i.e., the Smith Watson and Topper

(SWT) fatigue damage parameter [51].

3. Results and discussion

3.1. Thermal stress analysis

Fig. 6 shows the field of residual stress, which is related to the FSW process and obtained at the end of thermo-mechanical analysis (releasing step). Furthermore, points A1, B1, and C1, and A2, B2, and C2 positioned along the fronts of the lateral and central cracks, respectively, are used to measure the crack size with respect to the initial size during propagation. Points C1 and C2 are positioned at the middle of the fronts of lateral and central cracks, respectively. Otherwise, measuring points A1, A2, B1, and B2 are related to the intersection of the crack fronts with the free surfaces of the specimen.

In the thermo-mechanical analysis, the heat flux generated during the simulation of the welding process heats the material of the weld zone to a high temperature. Thereafter, the material that surrounds the weld zone prevents the expansion of the heated metal by exerting a compressive action; this phenomenon produces plastic yielding in the weld area. Furthermore, following the cooling of the joint, a contraction of the metal occurs along the direction of the welding path (longitudinal); this contraction is counteracted by the surrounding base metal. This contrasting actions lead to the formation of residual tensile stresses (weld bead) and residual compressive stresses (exterior of weld bead material) at the welded joint domain. Equilibrium is achieved by combining these stresses in the areas that immediately surround the weld bead. This peculiarity of the welding process can be clearly distinguished by an inspection of the residual stress distribution shown in Fig. 7. The figure shows numerical and experimental [10] residual stress profiles at the midline of thickness by the end of the releasing step for the uncracked configuration. In particular, the solution adopted in this case is obtained from a model where only hexahedral elements (C3D8) are used [25].

The residual stresses obtained with the numerical simulation include only those in the longitudinal direction because the only experimental data available for comparison are calculated in that direction.

The geometry, loads, and boundary conditions that are considered to simulate the fatigue crack propagation that occurs on the uncracked model are shown in Fig. 8. The fatigue load (24 kN), applied with a uniform distribution of tractions on the upper surface of the specimen (Fig. 8), causes a stress equal to 100 MPa. A thermal load equal to 25 °C is applied to the entire domain. The stress ratio, R = 0.1, is applied to all cases in this study. Moreover, the residual stress field is contained in the whole domain.

If the remote load is applied to the specimen, then a stress state is generated. This stress, as well as the residual stress, is distributed throughout the domain; the sum of these two stresses represents the overall stress (see Fig. 9).

3.2. Fatigue crack growth: Vasudevan's approach

The calculation of the total stress is developed in two steps. In the first step (step0), only the constraints applied on the crack faces are removed (the crack can open), whereas in the second (step1), the fatigue load is also applied. At the end of the first step, the residual stresses are redistributed throughout the domain; at the end of the second step, the overall stress is calculated.

Therefore, the total stress is the sum of the redistributed residual stress (for opening the crack) and the stress generated by the applied remote load. The yield strength value is used as the upper limit of the scale adopted (shown in red). It is noteworthy that in this case, the cracks are modelled as sharp, and the material behaviour is linear–elastic. Accordingly, overall K_I obtained through numerical analysis is shown in Fig. 10a and b. Unfortunately, only few experimental data are available for the comparison with the numerical results. Specifically, there are no experimental results available for the central crack; for the lateral crack, only few crack

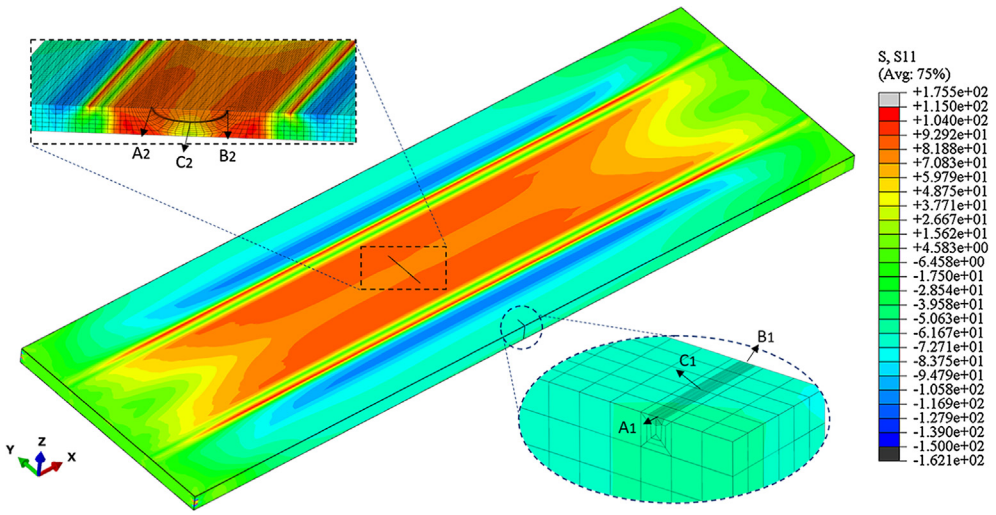

Fig. 6. Residual stress scenario (MPa) produced at the end of thermo-mehanical analysis.

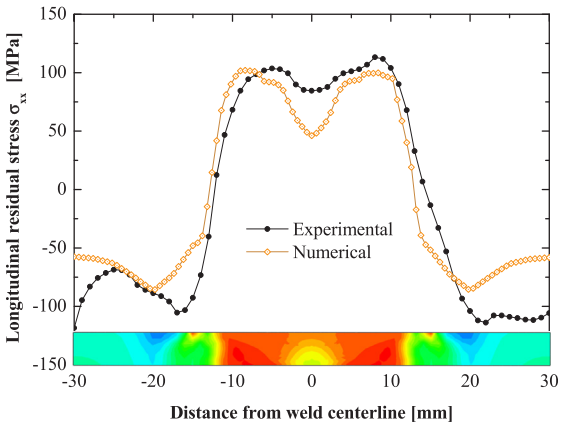

Fig. 7. Residual stress profiles evaluated at section containing central crack.

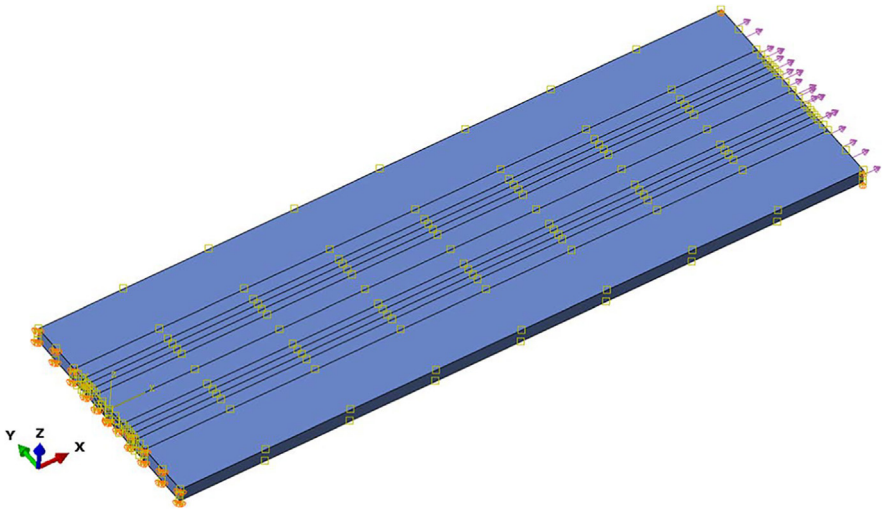

Fig. 8. Specimen model highlighting the boundary and loading conditions.

growth rates are recorded by the two crack gauges installed symmetrically with respect to the XY plane and close to the lateral crack front [10].

It can be observed that the highest SIF values can be found at approximately half the length of the crack fronts of both the lateral and central cracks where the constraint is higher.

3.3. Non-singular T-stress as constraint parameter

T-stress represents a stress parallel to the crack faces at the crack front [24]. Its magnitude can alter not only the size and shape of the plastic zone, but also the stress triaxiality ahead of the crack front. The T-stress is a parameter that can be numerically calculated by adopting a linear–elastic behaviour for the material. If the T-stress is used as a constraint parameter in a non-linear analysis, then its value is calculated from a linear–elastic model by applying the same loads that are employed in the non-linear analysis [24]. In general, the T-stress has larger domain dependence or contour dependence than J-integral and stress intensity factors, as similarly stated in the ABAQUS manual [24]; accordingly, the contour integral domain must completely include the plastic zone ahead of the crack front. In this simulation, standard blocks are employed to model the cracks by introducing up to seven contours to determine the value of the contour integral. This value must be approximately constant from one contour to the next. Thus, the T-stress values shown in Figs. 12 and 13 are derived from the fourth contour (Fig. 11) of the cracked mesh.

In Fig. 12(a) and (b), the T-stress along the normalised lateral and central crack fronts, respectively, are shown. Because of scaling, only the first 30 fatigue crack propagation steps are plotted. In Figs. 12 and 13, all the T-stress values indicated along the ordinate axis are dimensionless. These values are obtained by means of the stress biaxiality ratio, T/σ, where σ is the remote tensile load. On the abscissa axis, the dimensionless length of the crack fronts is shown. It may be noted that for the central crack, this constraint parameter changes along the crack front from the middle to the free surface; however, it does not affect the lateral crack, except in step1, where the central crack is considered as a surface crack. Furthermore, negative T-stresses favour the development of plasticity,

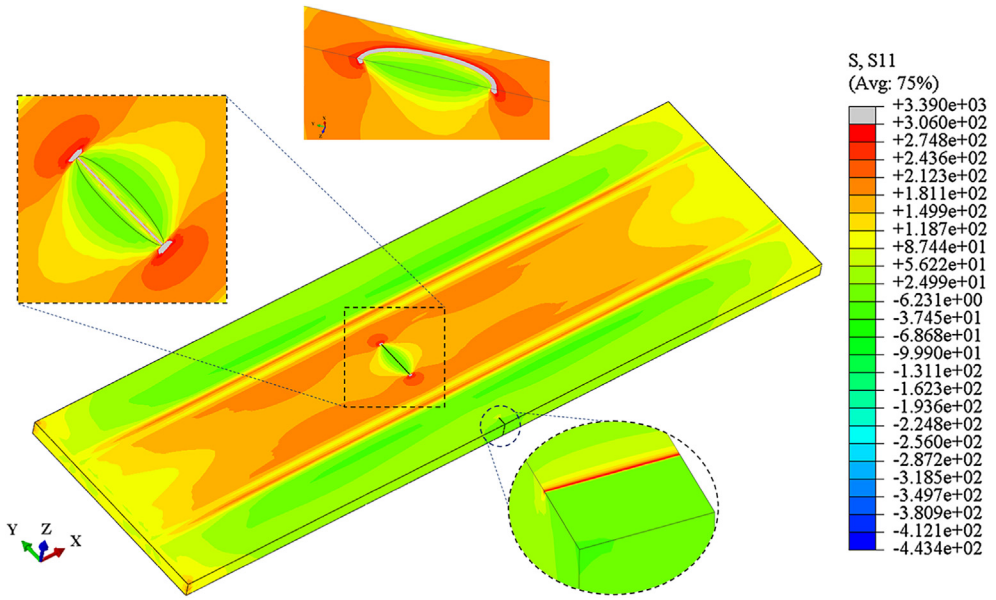

Fig. 9. Overall stress (MPa) scenario highlighting the cracked regions (step0).

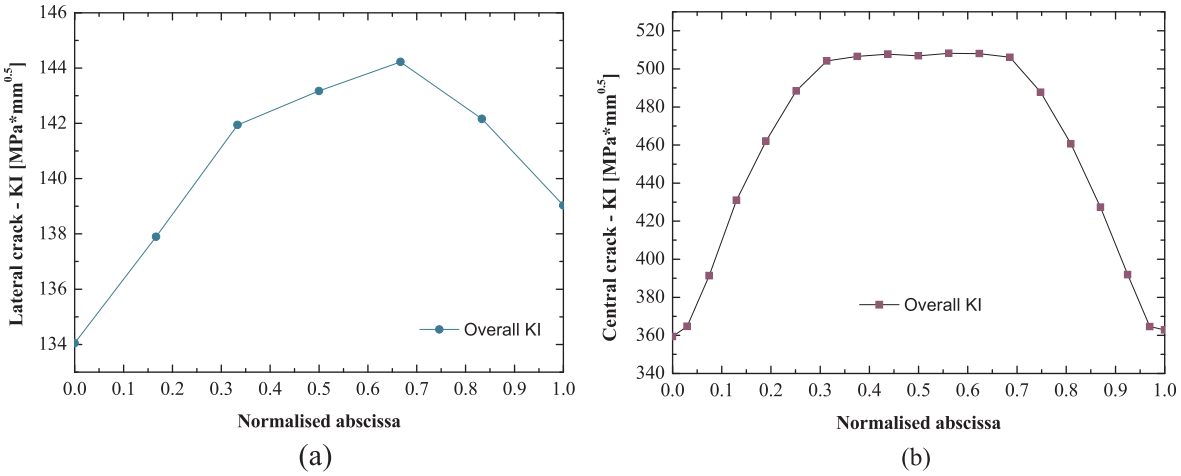

Fig. 10. Overall K_I (MPa) calculated for the (a) lateral and (b) central crack at step0.

whereas the positive values, especially the high T-stresses, are conducive to faster crack growth, which restricts yielding [55].

Regarding the T-stress values reported in Fig. 12(a), the special case of T = 0 corresponds to the small-scale yielding limit. The plastic zone is indeed a negligible fraction of the crack length and size of the body; the singular term uniquely defines the near-tip fields. It is noteworthy that a single-parameter description is rigorously correct only for T = 0. Hence, the plastic zone is considerably small with respect to the crack length and sizes of the tested specimen. In all the remaining steps, both for the lateral and central cracks, the T-stress values are negative; this causes a relaxation in the stress field surrounding the crack front. The last steps of the fatigue crack propagation for both lateral and central cracks are shown in Fig. 13(a) and (b).

In Figs. 12b and 13b, it is evident that the lower negative values of T-stress are in correspondence with the nodes closer to the free surfaces, where a lower relaxing of the constraint is observed, especially for the first 20 steps; the curves tend to become more flat after that number of cycles.

It is further noted in Step35 that for both lateral and central cracks, overall, the negative T-stress values increase. Consequently, a stronger plasticisation along the crack fronts and a further decrease in the constraint effect in the middle of the central crack are expected.

It must be recalled that T-stress is an elastic parameter. Hence, the T-stress values highlighted in Figs. 12(a), (b) and 13(a), (b) are obtained from a numerical simulation that considers a linear elastic behaviour of the material and adopts Vasudevan's equation as a crack growth law. Moreover, the boundary and loading conditions are the same as those shown in the linear–elastic case.

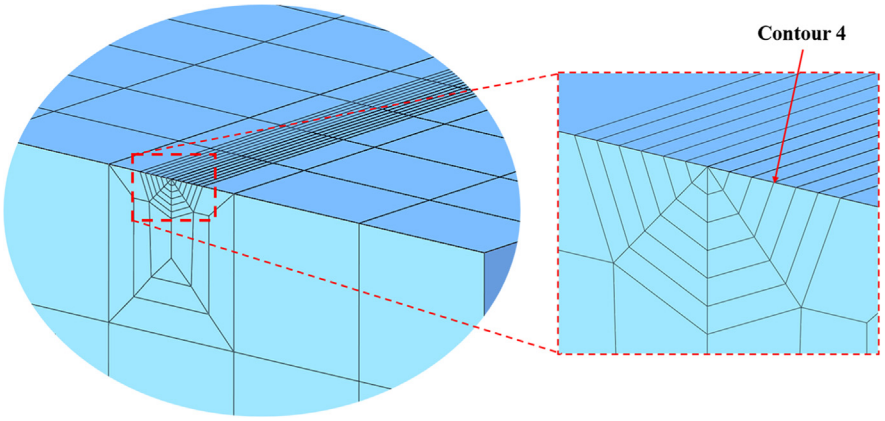

Fig. 11. Highlight of contour ring (red arrow) where T-stress is calculated (lateral crack). (For interpretation of the references to colour in this figure legend, the reader is referred to the web version of this article.)

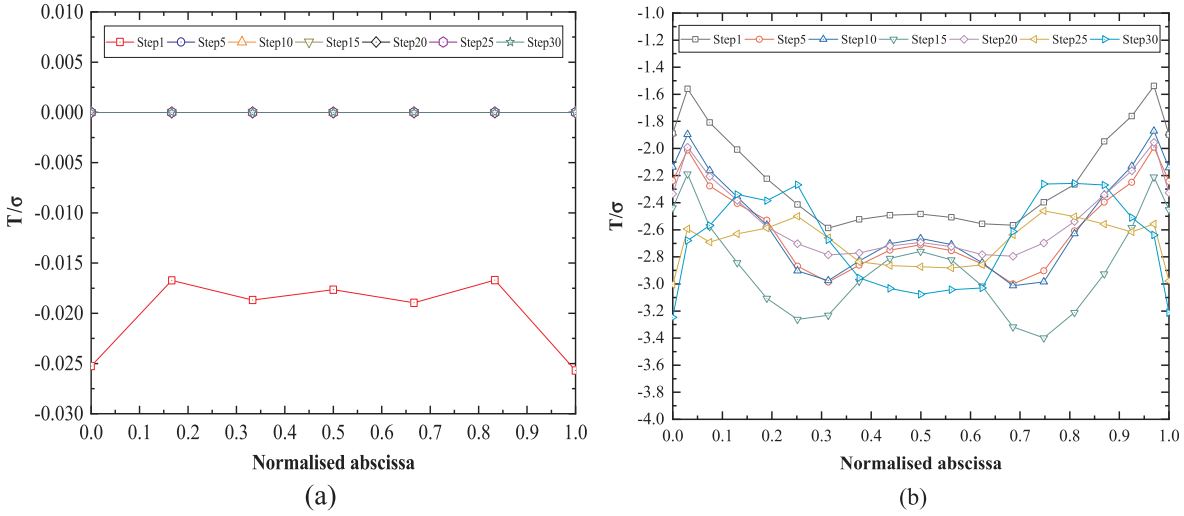

Fig. 12. T-stress distribution along the fronts of (a) lateral and (b) central cracks.

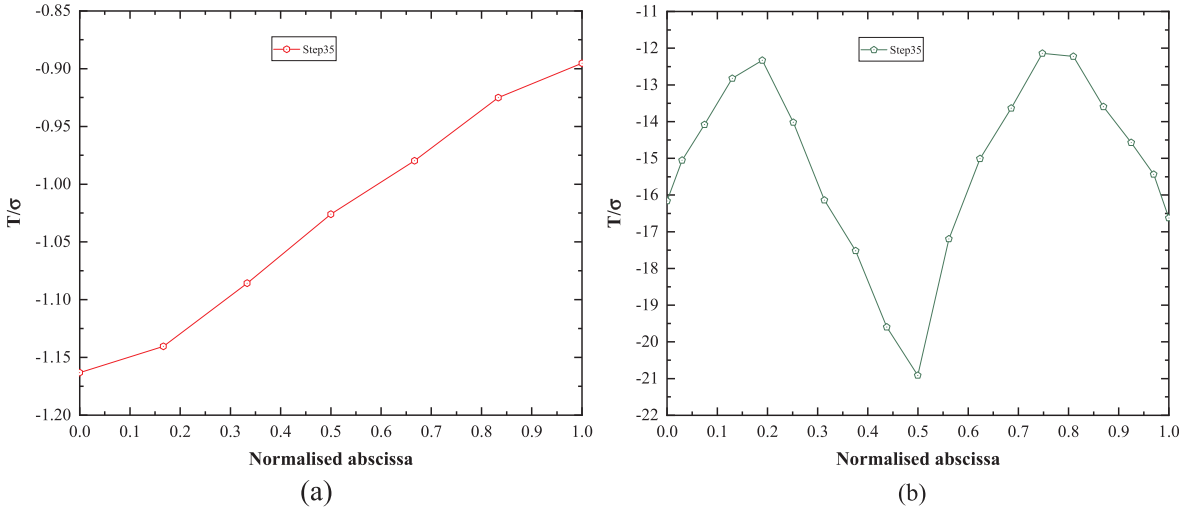

Fig. 13. T-stress distribution along (a) lateral and (b) central crack fronts for the last step of fatigue crack propagation.

3.4. Fatigue crack growth: The KE approach

The geometry of the FE model, as well as the solution of thermo-mechanical analysis (residual stress field), are used as starting points for the non-linear analysis; moreover, this model is employed for both cases of the study. Compared with the case of fatigue crack propagation of the linear–elastic analysis, the Kujawski–Ellyin and UniGrow models only change the crack front modelling and material behaviour (non-linear). In Fig. 14, only stresses acting along the X direction are plotted because the fatigue load is applied in that direction. In the analysis, each increment in the crack size can be divided into two numerical steps. In the first step (step0), the constraints applied on the crack faces are removed and a redistribution of residual stresses occurs; in the second (step1), the fatigue load is also applied.

In Fig. 15, the propagation results of the lateral and central cracks are shown. The most significant result is related to the lateral crack in which there is no propagation. In reality, the threshold limit imposed by ΔK_{th} is not exceeded by all nodes positioned on the crack front. This effect is induced by the compressive residual stress field that acts in that region; this stress field also produces a closure effect.

The increase in crack size, evaluated through measuring points A1 and B1, and A2 and B2, is shown in Fig. 15; these points are related to the intersections between the free surfaces of the specimen and the lateral and central crack fronts, respectively. Moreover, the increase in crack size, through measuring points C1 and C2, which are related to the middle of the lateral and central crack fronts, is also shown in Fig. 15. It is noteworthy that during approximately the first 500 cycles, point C2 increases at a higher rate than points A2 and B2; whereas, during the remaining cycles, points C2, A2, and B2 increase at a similar rate. Accordingly, the final aspect ratio of the central crack is consistent with the post-mortem aspect ratio of the corresponding experimental crack. Furthermore, as for the lateral crack, the simulation does not highlight any propagation. Instead, experimentally, a sudden acceleration in the lateral crack front, in correspondence with the free surfaces, is measured by two crack gauges applied ahead of the lateral crack front [10]. In this case, the behaviour of the lateral crack is not reproduced by the non-linear analysis, whereas it seems to better agree with the solution derived through the linear–elastic analysis. Here, the closure phenomenon performs a key function; an effective value of ΔK_{th} should be considered.

3.5. Fatigue crack growth: UniGrow approach

The unified two-parameter driving force model (UniGrow) considers ΔK_{tot} and $K_{max,tot}$ as applied stress intensity factors. These parameters account for the effect of local crack front stresses and strains on the fatigue crack growth. In this way, it becomes possible to predict the effect of the residual stresses and their mean, which are induced by cyclic loading [51]. Similarly, in the previous case in which Mode I is dominant, principal stress component S11 is plotted in the insertion phase of the crack (Fig. 16). Such stresses exhibit good agreement with those obtained by the KE model although the corresponding process zones are modelled differently. This behaviour is certainly because of the value of the fatigue load applied in these cases. As mentioned above, in the UniGrow technique, as well as the KE approach, each crack increment can be separated into two numerical steps.

The principal stresses related to the final configuration of the cracked specimen with two cracks are shown in Fig. 17. Moreover, in this case, the stresses acting along the X direction are considered. The central crack, regarded as a through-thickness crack and single crack front from hereon, is divided into two new crack fronts. Numerically, this aspect is modelled by using the technique

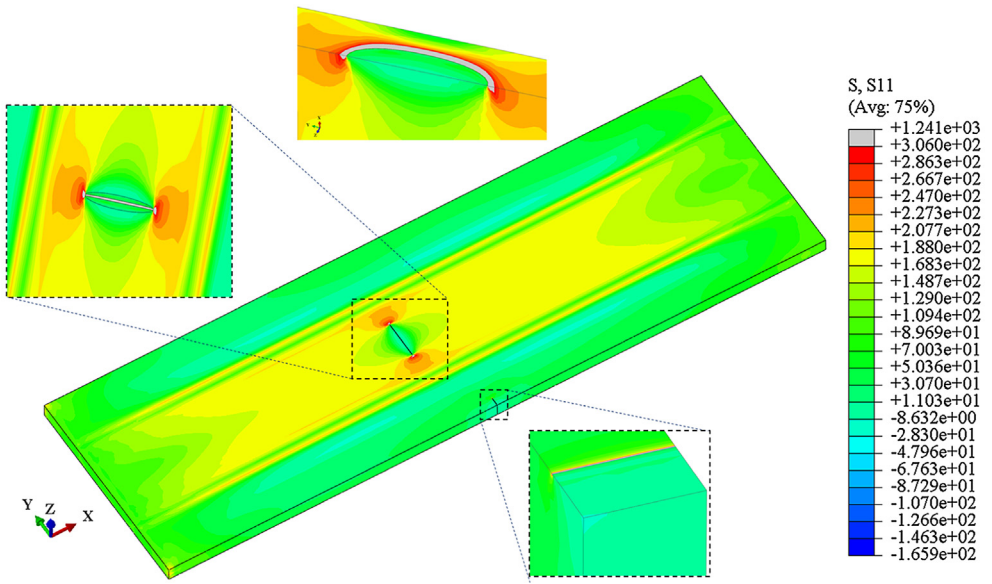

Fig. 14. Principal stress distribution (MPa) highlighting the cracked regions (step1).

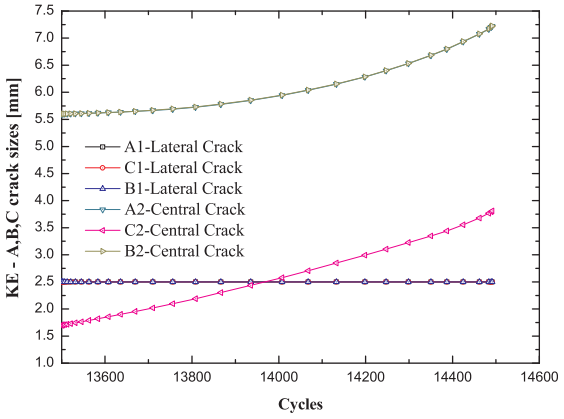

Fig. 15. Trends of measurement points A1, A2, B1, B2, C1, and C2, obtained during lateral and central crack propagation using KE approach.

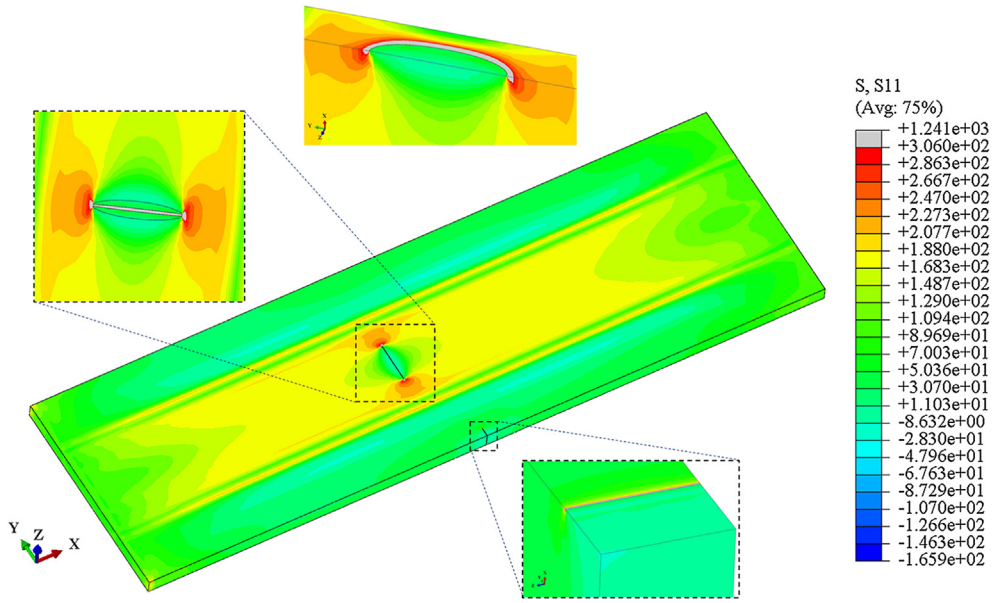

Fig. 16. Stress distribution (MPa) for the initial configuration of cracked specimen after application of fatigue load as highlighted in cracked regions (step1).

reported in Ref. [56]. Thereafter, certain other steps of the fatigue crack propagation are performed until the number of cycles measured in the experimental test is attained. Furthermore, it is noteworthy that the overall stress field near the lateral crack front (Fig. 17) is not symmetric because the compressive residual stress field acting in that region is not symmetric.

The increase in crack size, evaluated through measuring points A1, B1, A2, and B2, is shown in Fig. 18. Such an increase is also evaluated at points C1 and C2 of the lateral and central cracks (Fig. 18), respectively. In this case, the central crack growth rate is considerably similar to that obtained through the KE model; the crack aspect ratio is similar. Moreover, some propagations of the lateral cracks can be observed. This behaviour can be explained by recalling that the UniGrow model assesses crack closure effects.

As previously mentioned, after the central crack becomes a through-thickness crack, some other propagation steps are simulated, which divide the central crack into two separate fronts. All nodes of the original central crack front do not change except for the last node positioned on the breakthrough surface; this must be duplicated to create two new crack fronts [56]. Otherwise, the fatigue propagation of the lateral crack can continue simply from the last configuration reached. Therefore, some propagation steps of the three crack fronts are run until the number of cycles provided by the experimental test of the lateral crack is reached (step18).

In Fig. 19, the stress plot (deformed scale) of the final configuration of the cracked model with three crack fronts is shown with some details of the central and lateral cracks.

In Fig. 20, the overall increase in the crack size, evaluated through several measuring points and related to the case with only two crack fronts, is shown. A good agreement among these curves can be observed in both central and lateral cracks. A more detailed information can be deduced from the graph of this figure by pulling out a part of its contents and showing it on different figures. In Fig. 21, the crack growth rates of the KE and UniGrow models of the lateral and central cracks, respectively, are plotted separately.

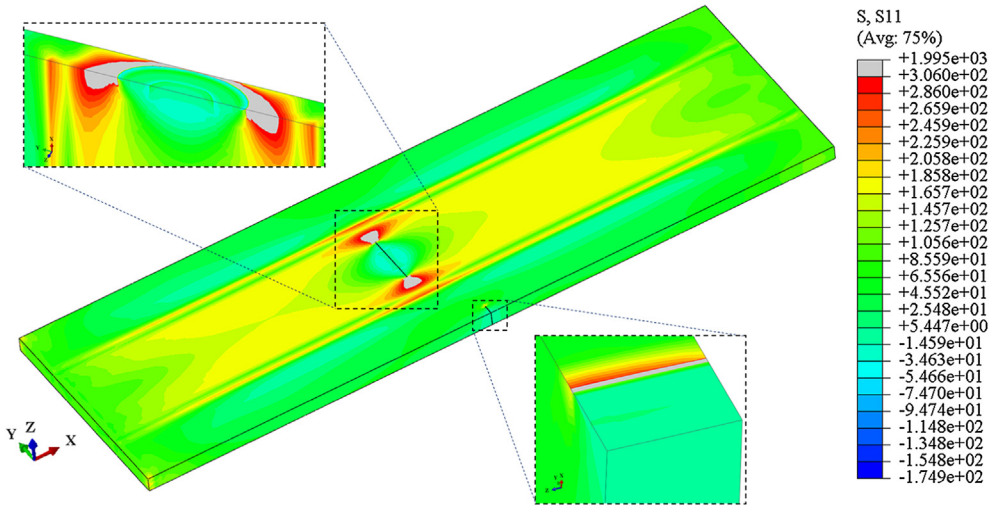

Fig. 17. Stress distribution (MPa) for final configuration of cracked specimen highlighting two-cracked regions (step35).

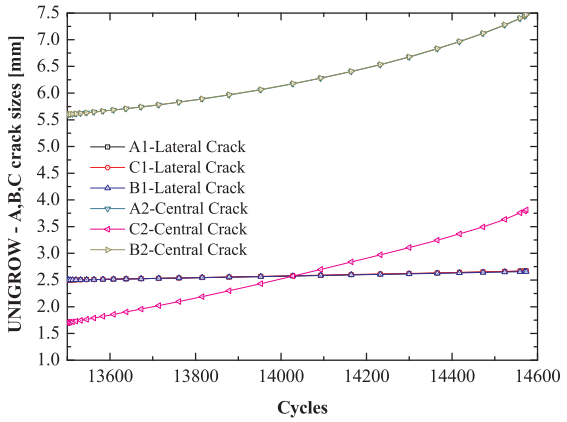

Fig. 18. Trends for measurement points A1, A2, B1, B2, C1, and C2, obtained during the lateral and central crack propagation of the considered UniGrow case.

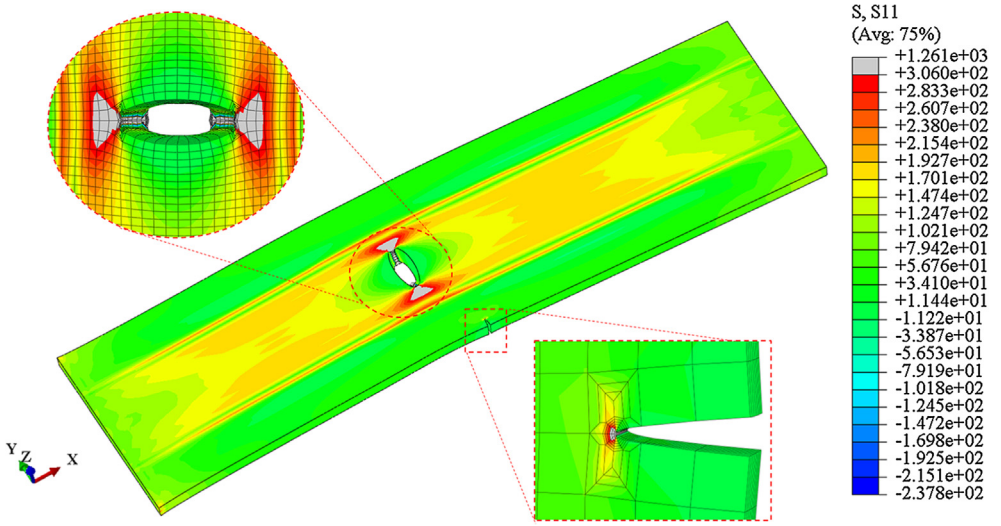

Fig. 19. Principal stress distribution (MPa) in final configuration. Three crack fronts, as well as crack regions (step53), are highlighted.

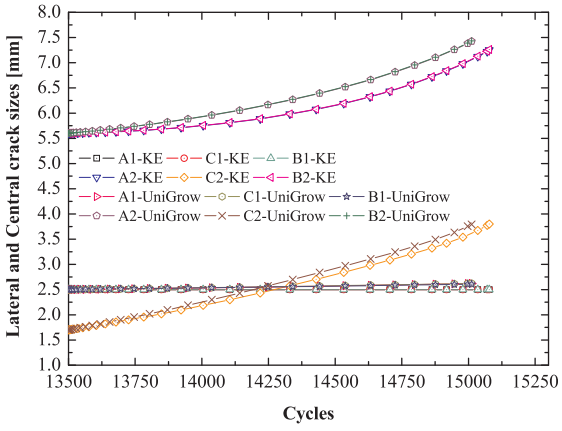

Fig. 20. Overall increase in crack size related to measuring points A1, B1, C1, A2, B2, and C2 for non-linear models (KE and UniGrow).

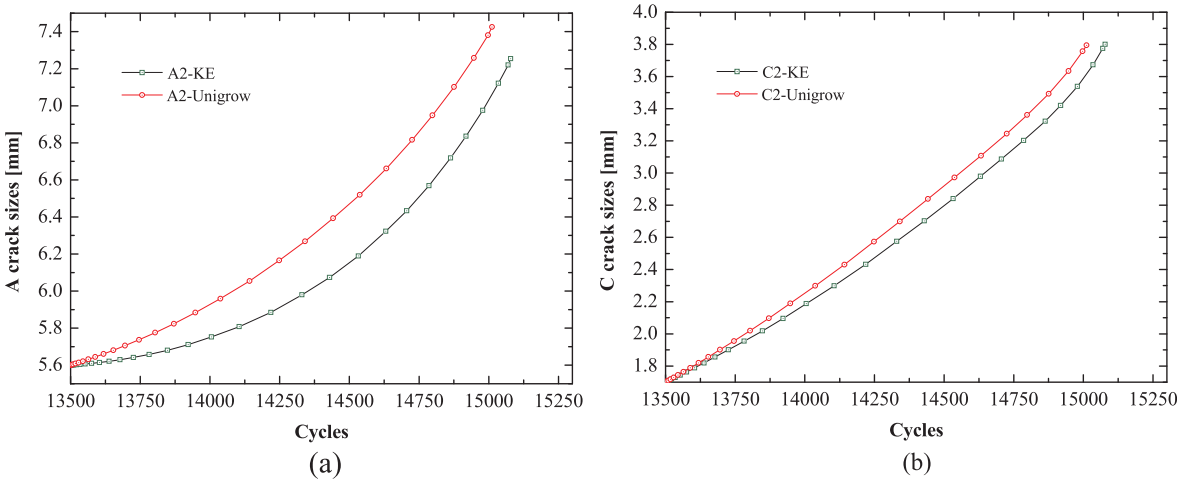

Fig. 21. Comparison between (a) A2 and (b) C2 crack sizes for KE and UniGrow approaches.

The comparison between the results shown in Fig. 21(a) and (b) shows an apparent and satisfactory agreement among the numerical data. The crack growth rates related to different non-linear models are similar in this case because the plastic zone is considerably small compared to the size of the crack (SSY). The non-linear models considered in this work substantially differ not

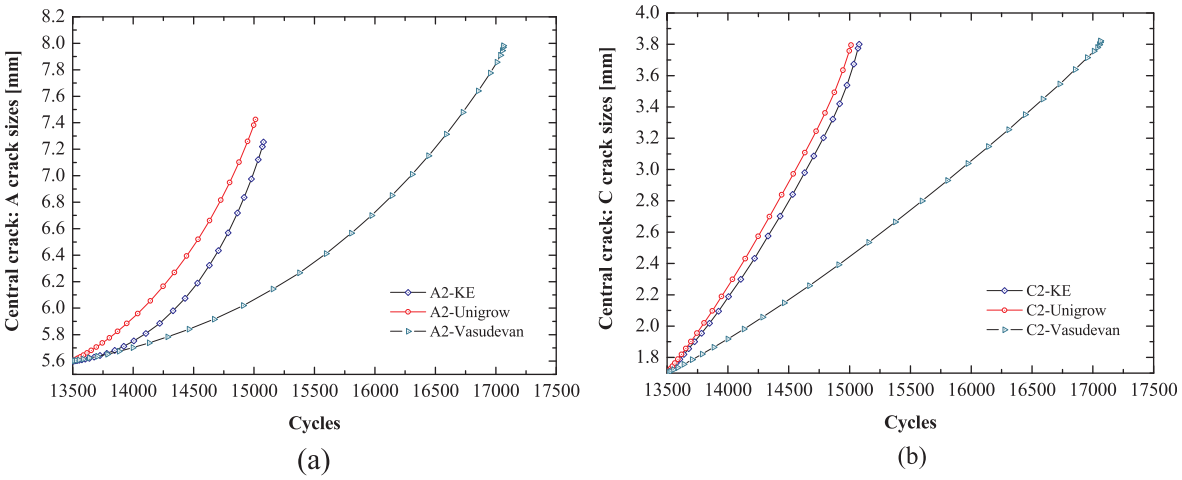

Fig. 22. Comparison between (a) A2 and (b) C2 crack sizes for KE, UniGrow, and Vasudevan approaches.

only because they are written as different equations, but also because they are based on different process zone definitions. Indeed, the KE model considers a smaller process zone than the plastic cyclic zone, whereas in the UniGrow model (as proposed by the authors), the process zone coincides with the extension of the cyclic plastic zone. Consequently, a larger process zone results in greater damage, which leads to fewer cycles to arrive at the estimated endpoint of the fatigue crack propagation.

The crack growth rates in the linear and non-linear–elastic analyses are shown in Fig. 22(a) and (b); In these figures, the difference between the linear–elastic and non-linear approaches is evident. The linear–elastic model predicts not only more cycles, but also a different aspect ratio of the central crack. Indeed, the final increment of point A2, which is related to the elastic case, has a higher value than those in the non-linear analyses (Fig. 22(a)). Otherwise, the difference between the final increments in the size of the two measuring points (C2) positioned at the middle of the central crack front is minimal (Fig. 22(b)).

Finally, in Fig. 23, the comparison between the numerical and experimental results of the lateral crack is highlighted. Considering the UniGrow approach, a reasonable agreement is shown between the lateral crack growth rates (related to the numerical analysis) and the experimental crack growth rates. In the same figure, UniGrow (1) and UniGrow (2) refer to the lateral crack propagation before and after the central crack becomes a through-thickness, respectively. It is observed in Fig. 23 that a better agreement between numerical and experimental results can be obtained if a non-linear analysis is implemented. On the other hand, a linear elastic analysis produces an overestimation of the propagation life of the specimen under investigation.

4. Conclusions

In this work, the friction stir welding process and fatigue propagation of several three-dimensional cracks in the welded component are simulated using the FEM. The simulation of the FSW process is necessary to produce the residual stress field that is subsequently employed for the simulation of the fatigue crack propagation. In the latter case, three FE simulations are performed by modelling the material behaviour as both linear–elastic and non-linear. Moreover, when the fatigue crack propagation is simulated by considering a linear–elastic behaviour of the material, the crack front is sharply modelled. Otherwise, when the non-linear behaviour of the material is taken into consideration, the crack front is modelled to include the blunting effect. Accordingly, three different laws for fatigue crack propagation are implemented in this work. Regarding the central crack, a satisfactory agreement is observed by comparing several crack sizes obtained by a linear–elastic and two numerical non-linear analyses. Furthermore, with the UniGrow approach for the lateral crack, a better agreement between the experimental and numerical results, obtained by the non-linear analysis under the SSY conditions, is found.

Accordingly, the main conclusions of this work are highlighted as follows.

- The FSW process is simulated by means of the finite element approach and the CCFT; consequently, a realistic residual stress field is derived.
- A fatigue crack propagation model is implemented considering both the Vasudevan law and linear–elastic material behaviour.
- The constraint parameter is modelled by considering the non-singular T-stress.
- The fatigue crack propagation is generated by considering both the Kujawski–Ellyin law and non-linear material behaviour in the SSY.
- A fatigue crack propagation model is implemented by considering both UniGrow and the non-linear behaviour of material in the SSY.
- A better agreement between non-linear analyses and experimental results of the lateral crack is observed by considering the UniGrow model and SSY conditions.

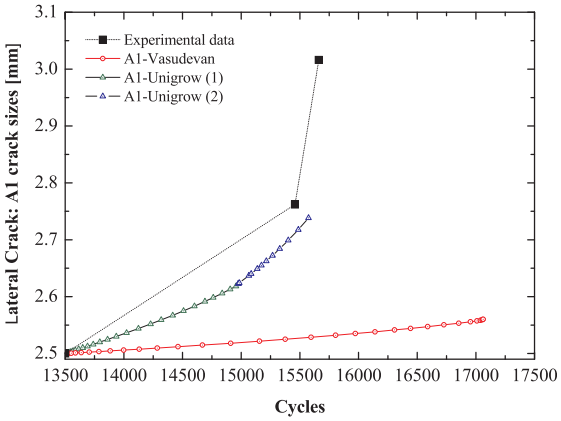

Fig. 23. Comparison between numerical and experimental results of lateral crack.

References

[1] Sukumar N, Chopp DL, Moran B. Extended finite element method and fast marching method for three-dimensional fatigue crack propagation. Eng Fract Mech 2003;70:29–48.
[2] Da Fonte M, Reis L, De Freitas M. Fatigue crack growth under rotating bending loading on aluminum alloy 7075-T6 and the effect of a steady state torsion 2015;80:57–64.
[3] Zerbst U, Ainsworth RA, et al. Review on fracture and crack propagation in weldments – a fracture mechanics perspective. Eng Fract Mech 2014;132:200–76.
[4] Dong P, Zhang J. Residual stresses in strength-mismatched welds and implications on fracture behavior. Eng Fract Mech 1999;64:485–505.
[5] Veljic Darko M, et al. A coupled thermo-mechanical model of friction stir welding. Therm Sci 2012;16:527–34.
[6] Citarella R, Cricrì G. A two parameter model for crack growth simulation by combined FEM-DBEM approach. Adv Eng Softw 2009;40:363–77.
[7] Živojinović D, Đurđević A, Grbović A, Sedmak A, Rakin M. Numerical modeling of crack propagation in friction stir welded joint made of aluminium alloy. Proc Mater Sci 2014;3:1330–5.
[8] Zadeh M, Ali A, Golestaneh AF, Sahari BB. Three dimensional simulation of fatigue crack growth in friction stir welded joints of 2024–t351 Al alloy. J Sci Ind Res 2009;68:775–82.
[9] Citarella R, Carlone P, Lepore M, Palazzo GS. Numerical–experimental crack growth analysis in AA2024-T3 FSWed butt joints. Adv Eng Softw 2015;80:47–57.
[10] Citarella R, Carlone P, Sepe R, Lepore M. Hybrid technique to assess the fatigue performance of multiple cracked FSW joints. Eng Fract Mech 2016;162:38–50.
[11] Sonne MR, Carlone P, Palazzo GS, Hattel JH. Numerical modeling of AA2024-T3 friction stir welding process for residual stress evaluation, including softening effects. Key Eng Mater 2014;611–612:1675–82.
[12] Carlone P, Palazzo G. Influence of process parameters on microstructure and mechanical properties in AA2024-T3 friction stir welding. Trans Indian Inst Met 2013;64:213–22.
[13] Paulo RMF, Carlone P, Valente RAF, Teixeira-Dias F, Palazzo GS. Influence of friction stir welding residual stresses on the compressive strength of aluminum alloy plates. Thin-Walled Struct 2014;74:184–90.
[14] Dialami N, Chiumenti M, Cervera M, de Saracibar CA. Challenges in thermo-mechanical analysis of friction stir welding processes. Arch Comput Methods Eng 2017;24:189–225.
[15] Ferro P, Berto F, James MN. Asymptotic residual stresses in butt-welded joints under fatigue loading. Theor Appl Fract Mech 2016;83:114–24.
[16] Ferro P, Berto F. Quantification of the influence of residual stresses on fatigue strength of Al-alloy welded joints by means of the local strain energy density approach. Strength Mater 2016;48:426–36.
[17] Chao YJ, Qi XH. Thermal and thermo-mechanical modeling of friction stir welding of aluminum alloy 6061-T6. J Mater Process Manuf Sci 1998;7:215–33.
[18] Zhu XK, Chao. Numerical simulation of transient temperature and residual stresses in friction stir welding of 304 L stainless steel. J Mater Process Technol 2004;146:263–272.
[19] Chen CM, Kovacevic R. Parametric finite element analysis of stress evolution during friction stir welding. Proc Inst Mech Eng Part B: J Eng Manuf 2006;220:1359–1371.
[20] Li T, Shi QY, Li HK. Residual stresses simulation for friction stir welded joint. Sci Technol Weld Join 2007;12:634–40.
[21] Hattel JH, Sonne MR, Tutum CC. Modeling residual stresses in friction stir welding of Al alloys—a review of possibilities and future trends. Int J Adv Manuf Technol 2015;76:1793–805.
[22] He Xiaocong, Gu Fengshou. A review of numerical analysis of friction stir welding. Prog Mater Sci 2014;65:1–66.
[23] Gibson BT et al. Friction stir welding: process, automation, and control 2014;16:56–73.
[24] Dassault Systems, Simulia Corp 2011. Abaqus analysis user's manual, Version 6.12.1. Providence, RI, USA.
[25] Zencrack v8.2.2 – 12. Documentation. Zentech International Limited; 2017.
[26] Kujawski D, Ellyin F. A fatigue crack propagation model. Eng Fract Mech 1984;20:695–704.
[27] Noroozi AH, Glinka G, Lambert S. A two parameter driving force for fatigue crack growth analysis. Int J Fatigue 2005;27:1277–96.
[28] Bažant ZP, Estenssoro LF. Surface singularity and crack propagation. Int J Solids Struct 1979;15:405–26.
[29] Pook LP. A 50 year retrospective review of three-dimensional effects at cracks and sharp notches. Fatigue Fract Eng Mater Struct 2013;36:699–723.
[30] Pook LP, Campagnolo A, Berto F. Coupled fracture modes of discs and plates under anti-plane loading and a disc under in-plane shear loading. Fatigue Fract Eng Mater Struct 2016;39:924–38.
[31] Pook LP, Berto F, Campagnolo A. State of the art of corner point singularities under in-plane and out-of-plane loading. Eng Fract Mech 2017;174:2–9.
[32] Kujawski D, Ellyin F. On the size of plastic zone ahead of crack tip. Eng Fract Mech 1986;25:229–36.
[33] Schwalbe KH. Comparison of several fatigue crack propagation laws with experimental results. Eng Fract Mech 1974;6:325–41.
[34] Lepore M, Carlone P, Berto F, Sonne Mads R. A FEM based methodology to simulate multiple crack propagation in friction stir welds. Eng Fract Mech 2017;184:154–67. https://doi.org/10.1016/j.engfracmech.2017.08.024.
[35] Schmidt H, Hattel JH. Thermal modeling of friction stir welding. Scripta Mater 2008;58:332–7.
[36] Sonne MR, Tutum CC, Hattel JH, Simar A, de Meester B. The effect of hardening laws and thermal softening on modeling residual stresses in FSW of aluminum alloy 2024–T3. J Mater Process Technol 2013;213:477–86.
[37] Richards DG, Pragnell PB, Williams SW, Withers PJ. Global mechanical tensioning for the management of residual stresses in welds. Mater Sci Eng A 2008;489:351–62.
[38] Carlone P, Citarella R, Sonne MR, Hattel JH. Multiple crack growth prediction in AA2024-T3 friction stir welded joints, including manufacturing effects. Int J Fatigue 2016;90:69–77.
[39] Myhr OR, Grong O. Process modeling applied to 6082–T6 aluminum weldments. Part 1: reaction kinetics. Part 2: applications of model. Acta Metall 1991;39:2693–708.
[40] Sancho R, Cendon D, Galvez F. Mechanical behavior of AA2024-T3 sheet metal at different strain-rates and temperatures. Procedia Eng 2017;197:158–67.
[41] Sadananda K, Vasudevan AK. Short crack growth and internal stresses. Int J Fatigue 1997;19:S99–108.
[42] Citarella R, Carlone P, Sepe R, Lepore M. DBEM crack propagation in friction stir welded aluminum joints. Adv Eng Softw 2016;101:50–9.
[43] Forman RG, Shivakumar V, Cardinal JW, Williams LC, McKeighan PC. Fatigue crack growth database for damage tolerance analysis. Report: DOT/FAA/AR-05/15, U.S. Department of Transportation < http://www.tc.faa.gov/its/worldpac/techrpt/ar05-15.pdf > .
[44] SWRI Southwest Research Institute US. NASGRO Fracture Mechanics & Fatigue Crack Growth Software US; 2002 < http://www.swri.org/sites/default/files/industries/nasgro-materials.pdf > [accessed 10.09.02].
[45] Ellyin F. Crack growth rate under cyclic loading and effect of different singularity fields. Eng Fract Mech 1986;25:463–73.
[46] Kujawski D, Ellyin F. A fatigue crack growth model with load ratio effects. Eng Fract Mech 1987;28:367–78.
[47] Li DM, Nam WJ, Lee CS. An improvement on prediction of fatigue crack growth from low cycle fatigue properties. Eng Fract Mech 1998;60:397–406.
[48] Shi KK, et al. Prediction of fatigue crack growth based on low cycle fatigue properties. Int J Fatigue 2014;61:220–5.
[49] Jing Li, et al. Theoretical estimation to the cyclic yield strength and fatigue limit for alloy steels. Mech Res Commun 2009;36:316–21.
[50] Huffman PJ. A strain energy based damage model for fatigue crack initiation and growth. Int J Fatigue 2016;88:197–204.
[51] Noroozi AH, Glinka G, Lambert S. A study of the stress ratio effects on fatigue crack growth using the unified two-parameter fatigue crack growth driving force. Int J Fatigue 2007;29:1616–33.
[52] Antolovich SD, Saxena A, Chanani GR. A model for fatigue crack propagation. Eng Fract Mech 1975;7:649–52.
[53] Bae Park H, Mo Kim K, Whi Lee B. Plastic zone size in fatigue cracking. Int J Press Vessels Pip 1996;68:279–85.
[54] Edmunds TM, Willis JR. Matched asymptotic expansions in non-linear fracture mechanics-iii. In-plane loading of an elastic perfectly plastic symmetric specimen. J Mech Phys Solids 1977;25:423–55.
[55] Jie Tong. T-stress and its implications for crack growth. Eng Fract Mech 2002;69:1325–37.

[56] Maligno AR, et al. A three-dimensional (3D) numerical study of fatigue crack growth using remeshing techniques. Eng Fract Mech 2010;77:94–111.
[57] Cherepanov CP. Crack propagation in continuous media. Appl Math Mech 1967;31:476–88.
[58] Rice JR. A path independent integral and the approximate analysis of strain concentrations by notches and cracks. J Appl Mech 1968;35:379–86.
[59] Brocks W. Plasticity and Fracture (Solid Mechanics and Its Applications). Springer International Publishing.
[60] Parks DM. A stiffness derivative finite element technique for determination of crack tip stress intensity factors. Int J Fract 1974;10:487–502.
[61] Parks DM. The virtual crack extension method for non-linear material behaviour. Comp Meth Appl Mech Eng 1977;1:353–64.
[62] DeLorenzi HG. Energy release rate calculations by the finite element method. General Electric Technical Information Series. Report No. 82CRD205; 1982.
[63] DeLorenzi HG. On the energy release rate and the J-integral for 3D crack configurations. J Fract 1982;19:183–93.
[64] Li FZ, Shih CF, Needleman A. A comparison of methods for calculating energy release rates. Eng Fract Mech 1985;21:405–21.
[65] Kuna M. Finite Elements in Fracture Mechanics (Solid Mechanics and Its Applications) 2013. Springer International Publishing.
[66] Shlyannikov VN, Zakharov AP, Yarullin RR. Structural integrity assessment of turbine disk on a plastic stress intensity factor basis. Int J Fatigue 2016;92:234–45.
[67] Hilton PD, Hutchinson JW. Plastic intensity factors for cracked plates. Eng Fract Mech 1971;3:435–51.
[68] Hutchinson JW. Singular behaviour at the end of a tensile crack in a hardening material. J Mech Phys Solids 1968;16:13–31.
[69] Shlyannikov VN, Tumanov AV, Zakharov AP. The mixed mode crack growth rate in cruciform specimens subject to biaxial loading. Theor Appl Fract Mech 2014;73:68–81.
[70] Hilton PD, Sih GS. Applications of finite element method to the calculations of stress intensity factors. Mech Fract Methods Anal Solut Crack Probl 1973;1:426–83.
[71] Hutchinson JW. Crack-tip singularity fields in non-linear fracture mechanics: a survey of current status. Adv Fract Res 1982;6:2669–84.